CZECH TECHNICAL UNIVERSITY IN PRAGUE
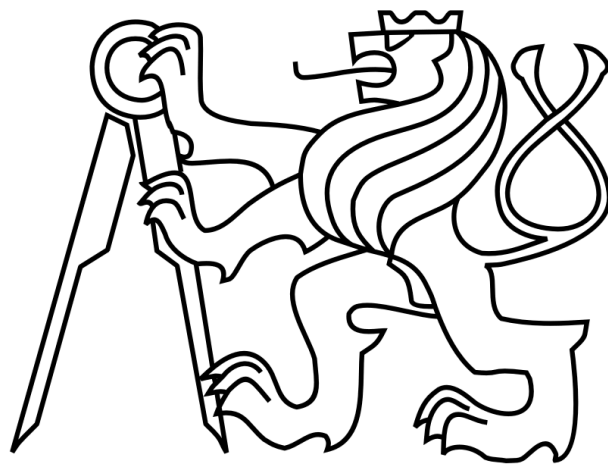
FACULTY OF NUCLEAR SCIENCES AND PHYSICAL ENGINEERING

Department of Physics

Experimental Nuclear and Particle Physics

Research thesis

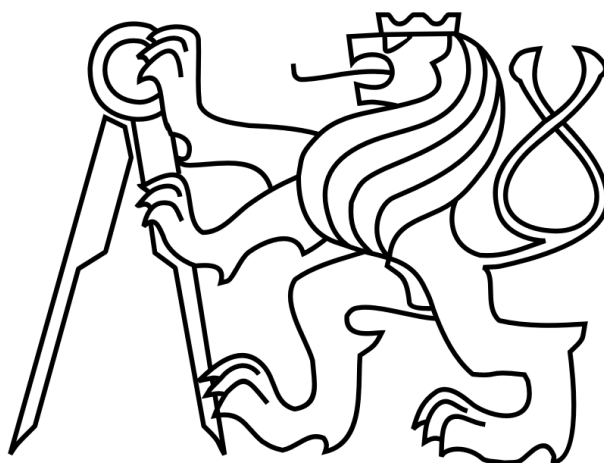## Study of jet shapes in Monte-Carlo generator JEWEL at RHIC

Author: Bc. Veronika Agafonova
Supervisor: RNDr. Jana Bielčíková, Ph.D.
Prague, 2019

ČESKÉ VYSOKÉ UČENÍ TECHNICKÉ V PRAZE

FAKULTA JADERNÁ A FYZIKÁLNĚ INŽENÝRSKÁ

Katedra fyziky

Experimentální jaderná a částicová fyzika

Výzkumný úkol

Studium tvaru jetů na urychlovači RHIC v Monte-Carlo generátoru JEWEL

Vypracovala: Bc. Veronika Agafonova
Školitel: RNDr. Jana Bielčíková, Ph.D.
Praha, 2019

Prohlášení

Prohlašuji, že jsem svůj výzkumný úkol vypracovala samostatně a použila jsem pouze podklady (literaturu, projekty, SW atd.) uvedené v přiloženém seznamu.

Nemám závažný důvod proti použití tohoto školního díla ve smyslu §60 Zákona č. 121/2000 Sb., o právu autorském, o právech souvisejících s právem autorským a o změně některých zákonů (autorský zákon).

V Praze dne ....

....
podpis

Poděkování

Děkuji RNDr. Janě Bielčíkové, Ph.D. za vedení mé práce, trpělivost a provedení jazykové korektury tohoto výzkumného úkolu.

Bc. Veronika Agafonova

Acknowledgement

Název práce:	**Studium tvaru jetů na urychlovači RHIC v Monte-Carlo generátoru JEWEL**
Autor:	Bc. Veronika Agafonova
Obor:	Experimentální jaderná a částicová fyzika
Druh práce:	Výzkumný úkol
Vedoucí práce:	RNDr. Jana Bielčíková, Ph.D.
	Ústav jaderné fyziky AV ČR, v.v.i.

Abstrakt: Jádro-jaderné srážky při energiích dosažitelných na urychlovači RHIC v BNL v USA jsou ideálním prostředím ke studiu jaderné hmoty v extrémních podmínkách vysokých teplot a hustot energií. Jednou z nejdůležitějších sond této jaderné hmoty je studium produkce jetů. Cílem tohoto výzkumného úkolu je popsat experiment STAR a diskutovat aktuální fyzikální výsledky týkající se studia tvaru jetů v jádro-jaderných srážkách na urychlovači LHC v CERN. Praktickou částí této práce je aplikace jetového algoritmu anti-kT a vybraných pozorovatelných popisujících tvar jetů na simulovaných datech s/bez modelu jaderného média na částicové úrovni v Monte-Carlo generátoru JEWEL při energii srážky 200 GeV v těžišťovém systému na nukleon-nukleonový pár a kinematickou oblast experimentu STAR na urychlovači RHIC. Získané výsledky tvaru jetů budou diskutovány v závislosti na energii (příčné hybnosti) jetu a centrality srážky ve vakuu a v jaderném médiu.

Klíčová slova: jet, jetový algoritmus, RHIC, JEWEL, kvarkovo-gluonové plasma

Title:	**Study of jet shapes in Monte-Carlo generator JEWEL at RHIC**
Author:	Bc. Veronika Agafonova

Abstract: The nuclear-nuclear collisions at energies attainable at the accelerator RHIC in BNL in the US are an ideal environment to study nuclear matter under extreme conditions of high temperature and energy density. One of the most important probes of the nuclear matter is study of the production of jets. The aim of the research thesis is to describe the STAR experiment and to discuss the actual physics results related to the jet studies in the nuclear-nuclear collisions at the LHC. The practical part of the thesis is focused on the anti-kT algorithm and the chosen jet shape observables on the simulated data with/without nuclear medium model at particle level in the Monte-Carlo generator JEWEL at the center of mass energy of 200 GeV per nucleon-nucleon pair. The obtained results for jet shapes will be discussed as a function of the transverse momentum of jet and the centrality in vacuum and nuclear medium.

Key words: jet, jet algorithm, RHIC, JEWEL, quark-gluon plasma

Contents

Chapter 1

Introduction to physics of nucleus-nucleus collisions

1.1 A phase diagram of nuclear matter

There are many experiments performing the research of nuclear matter called Quark-Gluon Plasma (QGP). The QGP is a state of matter existing in the conditions of extremely high temperature and density. It is assumed that after a few milliseconds after the Big Bang the universe was in a state of the Quark-Gluon Plasma.
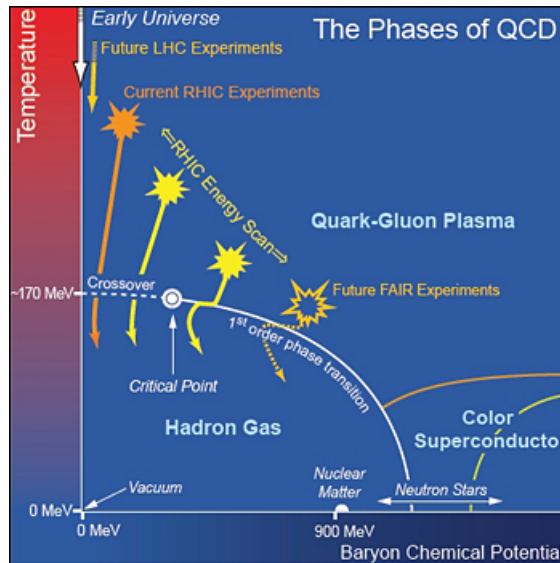
Figure 1.1: A phase diagram of nuclear matter showing the temperature T dependence on the baryon chemical potential μ_B [1].

Nowadays the QGP can be found in the centers of the compact stars or in the initial states of the nucleus-nucleus collisions that are studied at colliders. The hot and dense nuclear matter created in high energy collisions lives only for a short period of time, expands and cools down to form stable particles. There are currently two large experimental facilities where the necessary energies can be obtained. The Large Hadron Collider (LHC) at CERN that collides the lead nuclei. The highest

center-of-mass (CMS) (see Appendix A) energy obtained at the LHC was 5 TeV. The second facility is the Relativistic Heavy Ion Collider (RHIC) situated at Brookhaven National Laboratory. In contradiction to LHC, RHIC collides not only the nuclei of gold but many other nuclei such as copper, uranium, zirconium and ruthenium. RHIC has lower energies of the collisions in comparison to the LHC, it is $\sqrt{s_{\mathrm{NN}}} = 200$ GeV for Au and Cu, $\sqrt{s_{\mathrm{NN}}} = 100$ GeV for Zr and Ru, $\sqrt{s_{\mathrm{NN}}} = 193$ GeV for U.

Figure (1.1) presents a phase diagram of nuclear matter as the dependence of the temperature T on the baryon chemical potential μ_B. It can be seen, that the temperature of the transition from the QGP to hadron gas is nearly 170 MeV for zero value of the baryon chemical potential. The scientists are now trying to investigate the order of the phase transitions from the hadronic phase to the quark-gluon plasma and to the color superconducting phase. In case there is a possibility of having a cross-over for small chemical potentials and a first order for higher values of μ, when going from the hadronic to the QGP phase, the end of point of the first-order line is called the "critical point" of the QCD. In Figure (1.1) the idealized trajectories for RHIC beam energy scan and future Facility for Antiproton and Ion Research (FAIR) experiments are also shown in order to find the critical point of QCD.

1.2 Space-time evolution of nuclear collision

High-energy hadron collisions can be considered in terms of two space-time scenarios, one of which was invented by Bjorken [2] and another by Landau [3]. Consider now a central collision of two nuclei having a mass number A in the CMS frame with $\sqrt{s_{\mathrm{NN}}} = E_{cm}$ (see Appendix A). In this frame the nuclei are Lorentz-contracted and collide having a thicknesses of $d = 2R/\gamma_{cm}$, where $\gamma_{cm} = E_{cm}/2m_N$ is the Lorentz factor and m_N is the nucleon mass.

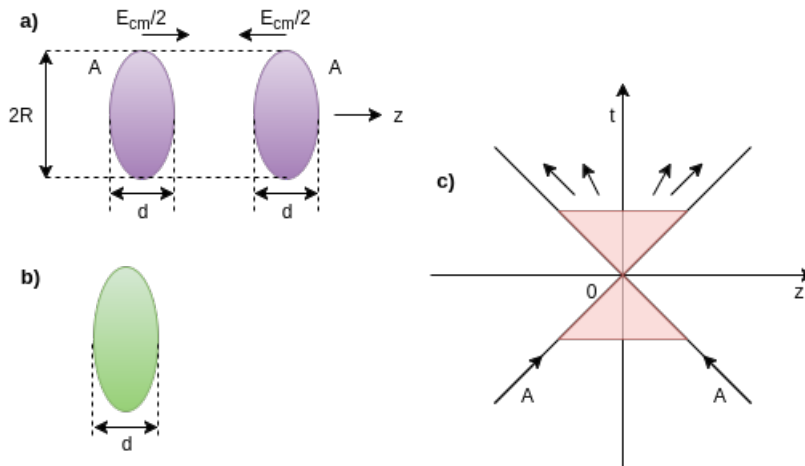Figure 1.2: A space-time view of a central collision of two heavy nuclei (A+A) in the Landau picture. a) Two nuclei approaching each other with relativistic velocities and zero impact parameter in the CMS frame. b) The slowing down of the nuclei with further interaction and particle production. c) The light-cone representation of the high-energy hadron collision in the Landau picture. The shaded area is the particle production area.

In the Landau picture (Figure 1.2), the colliding nuclei are considerably slowed down, producing particles mainly within the thickness of nuclear matter. Then, the expansion of the hot and baryon-rich system of particles occurs.

In the last decades, there is a considerable rise of the incident energy of the nuclei, the Landau model must be replaced by the Bjorken one (Figure (1.3)). The Bjorken scenario is based on the parton model of hadrons. The Bjorken scenario differs from the Landau picture by the time expansion of particle production and the existence of wee partons (gluons and sea-quarks), which carry much smaller momentum fraction of the nucleon in comparison to valence quarks.
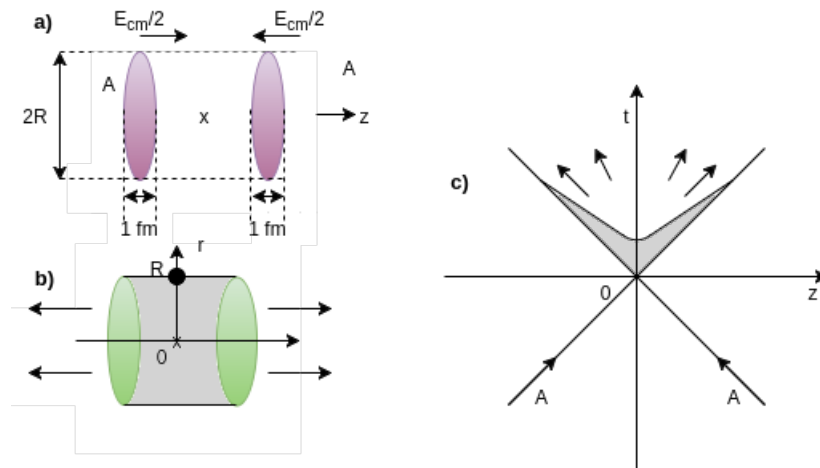

Figure 1.3: A space-time view of a central collision of two heavy nuclei $(A + A)$ in the Bjorken model. a) The central collision of two nuclei. b) Passage of the particles through each other. c) The light-cone representation of the high-energy hadron collision. The shaded area is the area of forming the highly excited matter.

Figure (1.3) shows a schematic figure of a central collision of two heavy nuclei in the light-cone representation. Firstly, we see the two nuclei approaching each other with the relativistic velocities in the center of mass frame (Figure (1.3 a)). As the collision is central, the value of the impact parameter is zero. As soon as the nuclei pass through each other, the highly excited matter with a small net baryon number between the nuclei is left (shaded area in Figure (1.3 b)). After the significant number of the virtual quanta and gluon coherent field configuration is excited, a proper time τ_{de}, typically a fraction of 1 fm, is needed to de-excite these quanta into real quarks and gluons. The state of matter for $0 < \tau < \tau_{de}$ is called the pre-equilibrium stage. As the τ_{de} is defined in the rest frame of each quantum, the τ can be then defined as $\tau = \tau_{de}\gamma$ in the center of mass frame. The γ stands for the Lorentz factor of each quantum. This implies the so called inside-outside cascade, meaning the slow particles are emerging first near the interaction point and then the fast particles far from the interaction point. This phenomenon is not included in the Landau model. In Figure (1.3 c) the light-cone representation of the hadron collision is shown. $\tau_0 < \tau_{de}$ stands for the proper time within which the system is equilibrated and depends on the basic parton-parton cross section and also on the density of partons produced in the pre-equilibrium stage.

It is known, that after the two nuclei collide, the fireball is created, which under-

goes different phases in its evolution. Figure (1.4) shows the space-time diagram of the relativistic collisions. The space-time evolution can be divided into three stages: pre-equilibrium stage and thermalization, hydrodynamical evolution and freeze-out, freeze-out and post-equilibrium.
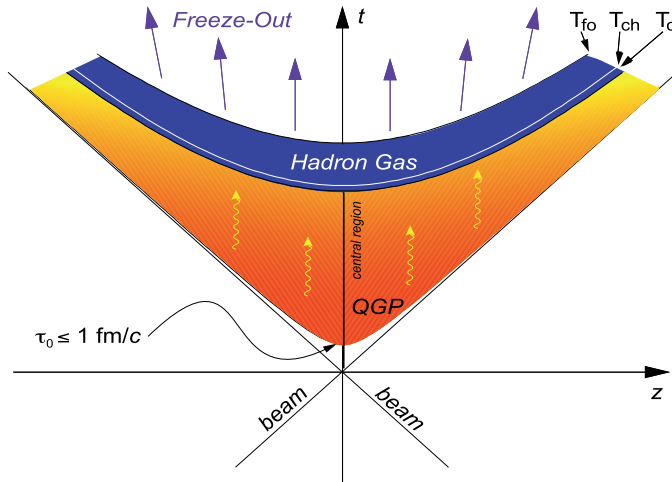

Figure 1.4: A space-time evolution of the relativistic heavy ion collision [4].

Pre-equilibrium stage and thermalization

For this stage $0 < \tau < \tau_0$ [5]. There are two models describing the entropy production in the central collision of ultra-relativistic heavy nuclei and subsequent thermalization. The first model is called coherent [5]. One of the example of the model is that the color strings and ropes are formed after the impact and subsequently decay into partons. After the real partons are produced, they move toward thermal distribution. Another example of the coherent model is based on the color glass condensate [6]. In the incoherent model [5], the semi-hard partons, or minijets, production due to the incoherent sum of collisions of incoming partons can be observed. After the minijets are produced, they interact with each other to form an equilibrated parton plasma.

Hydrodynamical evolution and freeze-out

For this stage $0 < \tau_0 < \tau_f$, where τ_f stands for the freeze-out time of the hadronic plasma. In this period the evolution of the thermalized QGP and its phase transition occur. After the local thermal equilibrium is reached at τ_0, the relativistic hydrodynamics can be used for the description of the expansion of the system. The expectation values of the equations of the conservation of energy-momentum tensor and baryon number,

$$\partial_\mu \langle T^{\mu\nu} \rangle = 0, \quad \partial_\mu \langle j_B^\mu \rangle = 0, \tag{1.1}$$

are taken with respect to the time-dependent state in the local thermal equilibrium. In case the system is approximated as a perfect fluid, the local energy density, ε, and the local pressure, P, parametrize the expectation values. Therefore, the Equation (1.1) is supplemented by the equation of state $\varepsilon = P(\varepsilon)$. Having the appropriate

initial conditions at $\tau = \tau_0$, the Equation (1.1) can predict the time development of
the system until it undergoes a freeze-out at $\tau = \tau_f$. In other case, when the system
cannot be approximated as a perfect fluid, the extra information is required.

Freeze-out and post-equilibrium

For this stage $\tau_f < \tau$. A space-time hyper-surface defines the freeze-out of the
hadronic plasma. As there is an increase of the mean free time of the plasma
particles in comparison to the time scale of the plasma expansion, the local thermal
equilibrium is no longer maintained. The freeze-out can be divided into 2 types. The
first is the chemical freeze-out, after which the number of each species is frozen, but,
nevertheless, the equilibration in the phase-space is still maintained. The other one is
the thermal equilibrium. In contradiction to chemical freeze-out, after the thermal
freeze-out occurs, the kinetic equilibrium is no longer maintained. Besides, there
could also be a difference in the temperature for the chemical and thermal freeze-
outs. The first one should occur at higher temperature followed by the second one.
After the evolution of the medium is finished, there is an increase in the distances
between the hadrons. Therefore, the hadrons leave the interaction region, but still
can interact in a non-equilibrium way.

1.3 Centrality of the collision

1.3.1 Centrality types

Nuclear collisions can be classified according to the size of the overlapping area that
is related to centrality. Centrality can be determined as:

$$c_b \equiv \frac{1}{\sigma_{innel}} \int_0^b P_{inel}(b') 2\pi b' db', \qquad (1.2)$$

where σ_{inel} is the inelastic nucleus-nucleus cross section, P_{inel} is the probability
that an inelastic collision occurs at the impact parameter b that is defined as the
difference between the positions od the nuclei centers. Depending on the values
of the impact parameter one can distinguish three types of collisions: central or
"head-on" collisions, peripheral and ultra-peripheral collisions (Figure 1.5). Central
collisions have the impact parameter $b \approx 0$, peripheral collisions have $0 < b < 2R$,
and ultra-peripheral collisions have $b > 2R$, where the colliding nuclei are viewed as
hard spheres with radius R.

The centrality dependence of various observables provides insight into their de-
pendence on the global geometry. As the energy loss of jets increases with the length
of the path traversed by the particles inside the quark-gluon plasma, it is larger in
central collisions.

1.3.2 Determination of centrality

In heavy-ion collisions the centrality of the collision and the impact parameter cannot
be directly experimentally measured, even though they are perfectly well-defined
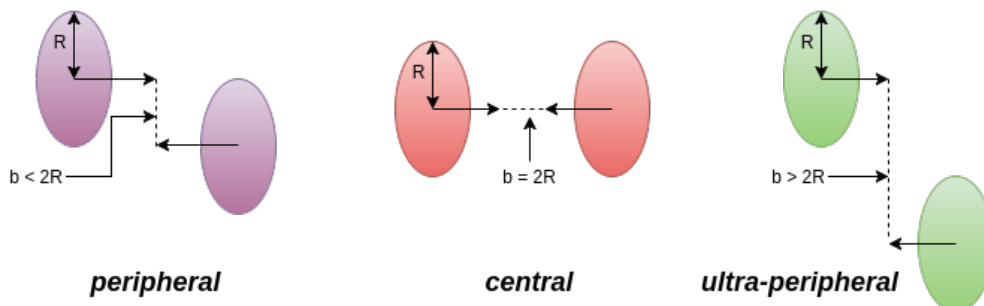quantities. There are two main methods to determine the centrality.

Figure 1.5: A schematic view of peripheral, central and ultra-peripheral collisions.

The first is to measure the particle multiplicity, which is proportional to the energy released in the collision. As the color force has an extremely short range, it cannot couple quarks that are separated by much more than nucleon's radius. The more central the collision is, the higher multiplicity of created particles it has. Therefore, the more tracks of the particles can be observed in the detector. The charged particle multiplicity distributions can be seen in Figure (1.6). The first 5% of the high minimum-bias multiplicity, N_{ch}, events corresponds to central collisions and the last 50% of N_{ch} corresponds to peripheral collisions.
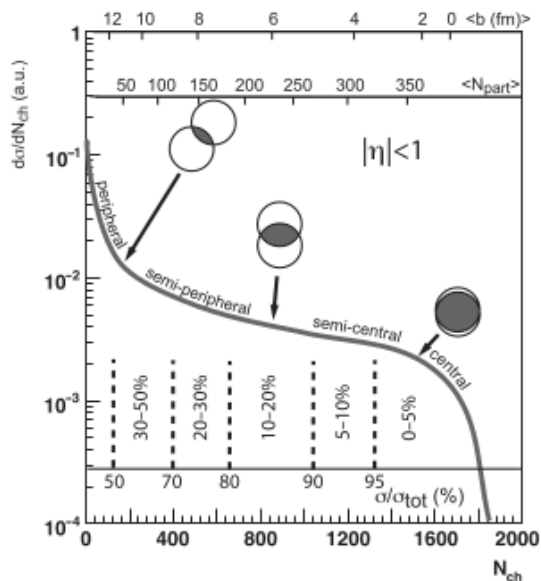

Figure 1.6: The measured charged particle multiplicity in Au+Au collisions at $\sqrt{s_{NN}} = 200$ GeV by the STAR experiment together with corresponding values of the impact parameter b, number of participants N_{part} in the collisions and fraction of geometrical cross-section σ/σ_{tot} [7].

Another way to determine the centrality is to measure the nucleons which do not participate in the collision (*spectators*). For this measurement the special Zero Degree Calorimeters (ZDC) (see Subsection 3.2.6 for more information) can be used. The number of the spectators for central and most peripheral collisions ~ 0, since

the nucleons in the colliding nuclei are not "kicked out" of the nuclei, therefore they
are not measured by ZDCs. There may also be different amount of spectators for the
same impact parameter b in the collisions of deformed nuclei having different orien-
tations of the spectators for the same impact parameter. The number of participant
nucleons can be evaluated using the semi-classical Glauber model [8].

1.4   Glauber model of nucleus-nucleus collisions

In order to describe the high-energy nuclear reactions and evaluate the total reaction
cross-section, the number of nucleons that participated in binary collision at least
once (participant nucleons), N_{part}, and nucleon-nucleon collisions, N_{coll}, the Glauber
model [8] is used. The Glauber model is a semi-classical model, which considers the
nucleus-nucleus collision as multiple nucleon-nucleon interactions (see Figure (1.7)).
That means there is an interaction between the nucleon of the incident nucleus and
the target nucleons with a given density distribution. The nucleons are assumed
to travel in the straight lines, which are not deflected after the collision. That
gives a good approximation at very high energies. As this model does not consider
the secondary particle production and possible excitations of nucleons, the nucleon-
nucleon inelastic cross section, σ_{NN}^{in}, is assumed to be the same as that in the
vacuum.

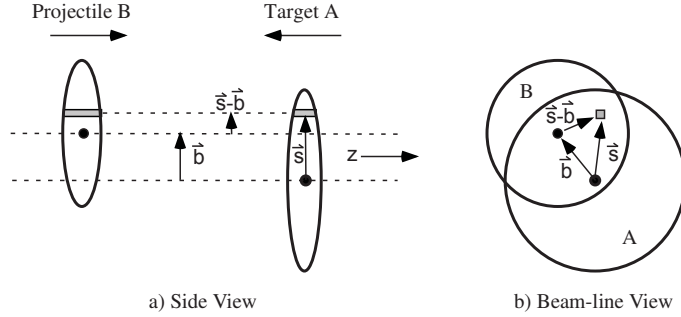a) Side View   b) Beam-line View

Figure 1.7: Geometry of a collision between nuclei A and nuclei B. with transverse (a)
and longitudinal (b) views [9].

In the Glauber model, the number of participant nucleons, N_{part}, and the number
of binary nucleon-nucleon collisions can be found as follows:

$$N_{part}(b) = \int d^2\vec{s}\, T_A(\vec{s}) \left(1 - \exp^{-\sigma_{NN}^{in} T_B(\vec{s})} \right)$$

$$+ \int d^2\vec{s}\, T_B(\vec{s}-\vec{b}) \left(1 - \exp^{-\sigma_{NN}^{in} T_A(\vec{s})} \right), \qquad (1.3)$$

$$N_{coll}(b) = \int d^2\vec{s}\, \sigma_{NN}^{in} T_A(\vec{s}) T_B(\vec{s}-\vec{b}). \qquad (1.4)$$

Here, the T_A is the thickness function defined as $T_A(s) = \int dz \rho_A(z, \vec{s})$, $\vec{b}$ is the impact
parameter, $\vec{s}$ is the impact parameter of all the pairs of incident and target nucleons,
z is the collision axis and ρ_A is the nuclear mass number density normalized to mass
number A.

Chapter 2

Tomography of medium with hard probes

2.1 Jet

The study of production of jets is one of the most important probes of nuclear matter under extreme conditions of high temperature and energy density. Jet is a collimated spray of hadrons originating from fragmentation of a hard parton created in the initial stage of the nucleus-nucleus collision and can be used for tomography of the nuclear matter and probe of a proton structure (Figure (2.1)). As jets mostly conserve the energy and the direction of the originating parton, they are measured in particle detectors and studied in order to determine the properties of the original quarks.
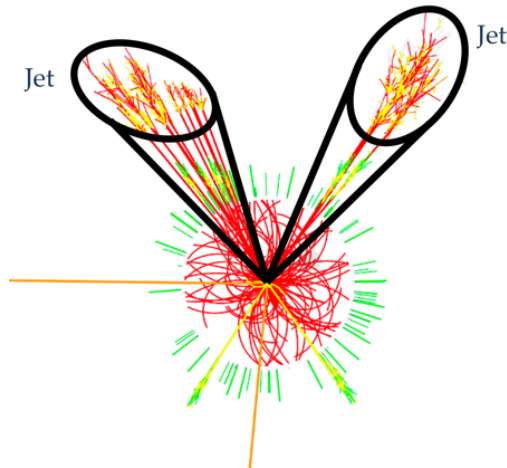

Figure 2.1: A schematic view of jet created in a heavy-ion collision [10].

Jets can be divided into two groups: regular or "soft-resilient" and less regular or "soft-adaptable". Having a regular jet can simplify some theoretical calculations as well as some parts of the momentum resolution loss caused by underlying event or UE (see Appendix B) and pile-up contamination. An infrared and collinear (IRC) safe algorithm (see Appendix B) can stimulate irregularities in the boundary of the final jet in the second type of the jets.

2.2 Jet measurement at the LHC

At the LHC the jet analysis is performed by the ATLAS, ALICE and CMS collaborations. The ATLAS and CMS do the high-p_T jets, while the ALICE is focused on the low-p_T jets. The summary of results of jet measurements performed by these experiments will be presented in this section.

2.2.1 Nuclear modification factor

The nuclear modification factor, R_{AA}, is a tool for probing of QGP quantitatively. It characterizes the particle production or jet production in nuclear medium. It is defined as:

$$R_{AA} = \frac{1}{\langle T_{AA} \rangle} \frac{\mathrm{d}^2 N_{AA}/\mathrm{d}y\mathrm{d}p_T}{\mathrm{d}^2 \sigma_{\mathrm{pp}}/\mathrm{d}y\mathrm{d}p_T}, \tag{2.1}$$

where $\langle T_{AA} \rangle$ is the nuclear thickness function accounting for increased flux of partons per collision in A+A collisions and it is estimated using Glauber model (see Section 1.4), $\mathrm{d}^2 N_{AA}/\mathrm{d}y\mathrm{d}p_T$ is the differential yield of charged particles in A+A collisions measured differentially in transverse momentum of tracks p_T and rapidity y (see Appendix A).
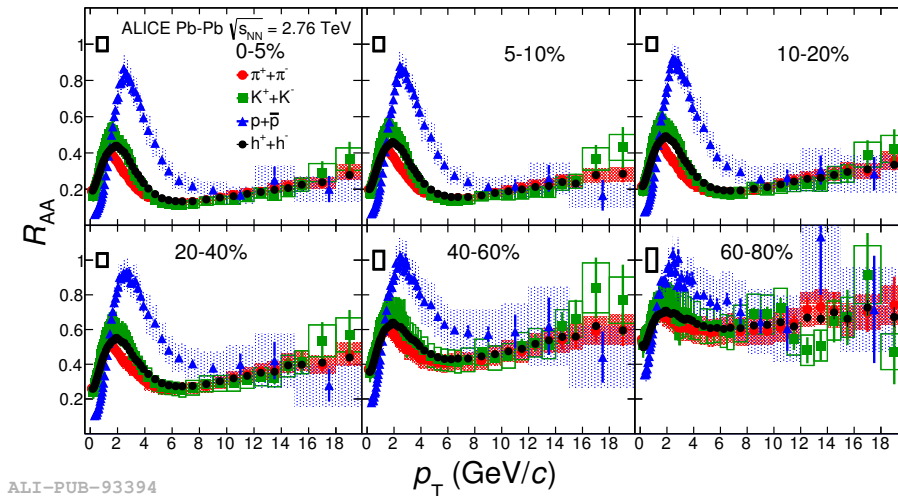

ALI-PUB-93394

Figure 2.2: Nuclear modification factor R_{AA} as a function of p_T in different centrality classes for pions, kaons and protons [11].

Figure (2.2) shows the nuclear modification factor for various particles in different centrality classes in Pb+Pb collisions at $\sqrt{s_{\mathrm{NN}}} = 2.76$ TeV performed by ALICE. It can be seen that all the particles are suppressed for $p_T > 10$ GeV/c, while for lower $p_T < 10$ GeV/c the particles are less suppressed for all centrality bins. The maximum value of the R_{AA} is reached between 2 and 4 GeV/c.

The nuclear modification factor of the anti-kT (see Section 4.2.2) jet as a function of p_T is presented in Figure (2.3). The results were obtained by the ATLAS collaboration for Pb+Pb collisions at $\sqrt{s_{\mathrm{NN}}} = 2.76$ TeV. The resolution parameter of the jet was chosen to be $R = 0.4$. As it can be seen, there is a weak increase of
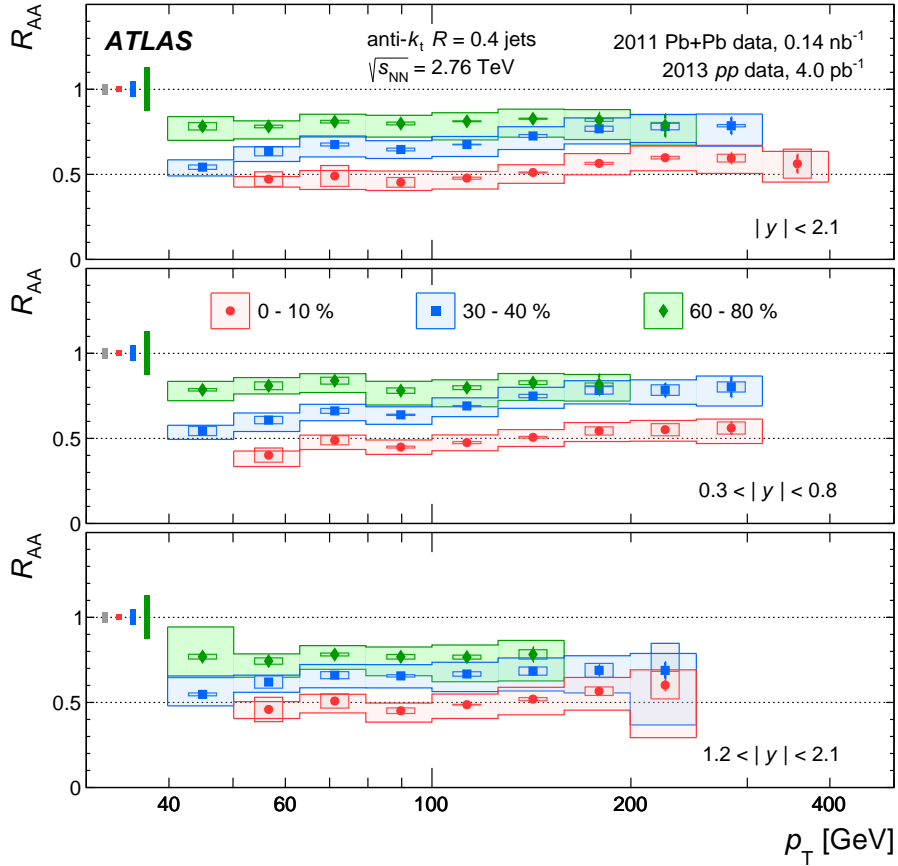
Figure 2.3: Jet R_{AA} as a function of p_T for different centralities. Each panel shows a different range in $|y|$ [12].

the R_{AA} with p_T for all but the most peripheral collisions. In the 0–10% and $|y| < 2.1$ centrality and rapidity intervals the R_{AA} is 0.47 at $p_T \approx 55$ GeV and then rises to 0.56 at $p_T \approx 350$ GeV.

2.2.2 Examples of jet measurements

There are several jet measurements that were made by the CMS collaboration [13]. Figure (2.4) shows an example of differential jet shape measurements in Pb+Pb and p+p collisions as a function of the distance from the jet axis for $p_T > 100$ GeV/c in different centrality regions. The bottom panel shows the ratios of differential jet shapes in Pb+Pb and p+p collisions in order to see the effect of the medium on jet shapes more clearly. The observed deviations from unity demonstrate modification of jet structure in the nuclear medium. In the most central collisions the abundance of transverse momentum fraction emitted at large radius $r > 0.2$ appears. This fact demonstrates a temperate broadening of the jets in the medium.

The experiments at the LHC also study the dijet production. Figure (2.5) shows the dijet assymetry ratio for 7 TeV p+p (a) and 2.76 TeV Pb+Pb collisions for several centrality classes measured by the CMS collaboration. Data are shown as black points. The histograms show (a) PYTHIA events and (b)–(f) PYTHIA events
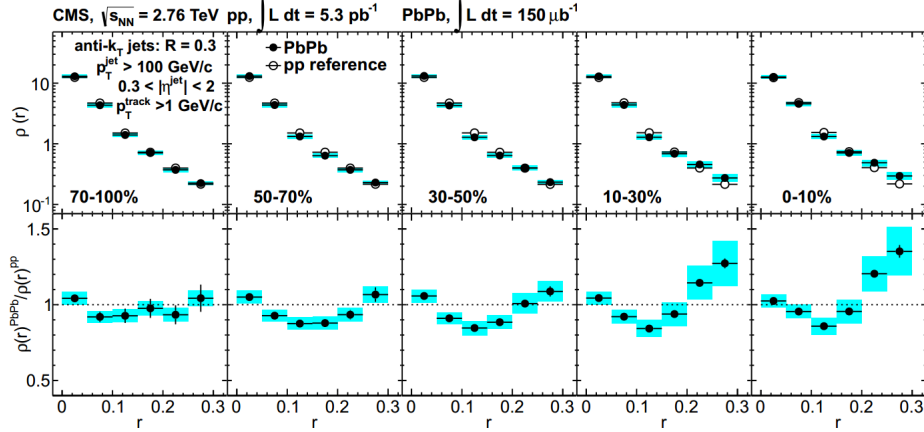
Figure 2.4: Top panel shows the differential jet shapes in Pb+Pb and p+p collisions. Bottom panel shows the ratio of jet differential jet shapes in Pb+Pb and p+p collisions [13].

embedded into Pb+Pb data. A good agreement between the data and event generator can be observed for (a) and the most pripheral collisions (b). It is also seen, that there is a small dependence of the dijet angular correlation on the centrality (c)–(f). The similar analysis was also performed by the ATLAS collaboration. An interested reader can find more information about the ATLAS analysis in [14].
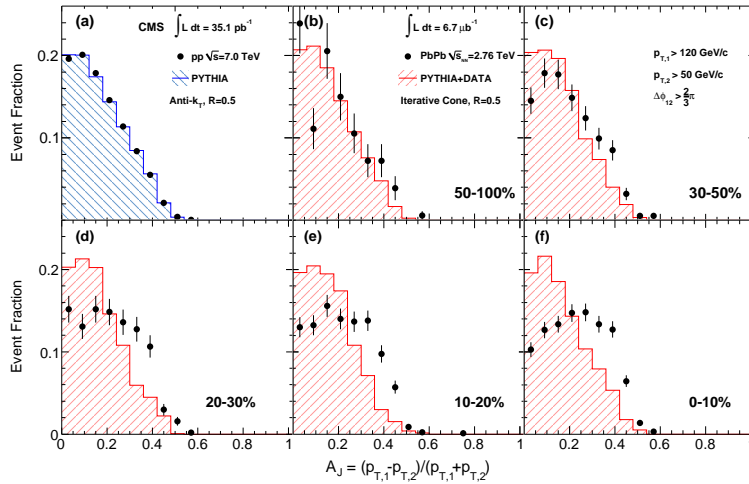

Figure 2.5: Dijet asymmetry ratio, A_j, for leading jets of $p_{T,1} > 120$ GeV/c with subleading jets of $p_{T,2} > 50$ GeV/c and $\Delta\phi_{12} > 2\pi/3$ for 7 TeV p+p collisions (a) and 2.76 TeV Pb+Pb collisions for different centrality classes [15].

2.3 Jet shapes

In order to probe the complimentary aspects of the jet fragmentation and constrain different aspects of the theoretical description of jet-medium interactions, different

observables related to shapes of jets are studied. In this thesis the attention will be paid to such jet shape observables as angularity, momentum dispersion and LeSub.

The *radial moment* (alternatively *angularity* or *girth*), g, probes the radial distribution of radiation inside a jet. It is defined as

$$g = \sum_{i \in jet} \frac{p_\mathrm{T}^\mathrm{i}}{p_\mathrm{T,jet}} |\Delta R_\mathrm{i,jet}|, \tag{2.2}$$

where p_T^i represents the momentum of the ith constituent and $\Delta R_\mathrm{i,jet}$ is the distance in $\eta \times \phi$ plane between the constituent i and the jet axis [16]. η stands for the pseudorapidity (see Appendix A) and ϕ is the azimuthal angle. This type of shape is sensitive to radial energy profile or broadening of the jet. In the collinear limit for the polar angle (see Appendix A) $\theta \to 0$ the radial moment becomes equivalent to jet broadening.

The next observable is *momentum dispersion $p_T D$* given by the equation:

$$p_T D = \frac{\sqrt{\sum_{i \in jet} p_\mathrm{T,i}^2}}{\sum_{i \in jet} p_\mathrm{T,i}}. \tag{2.3}$$

This observable measures the second moment of the constituent p_T distribution in the jet and is connected to hardness or softness of the jet fragmentation. In case of a large number of constituents and softer momentum the $p_\mathrm{T} D$ tends to 0, while in the opposite situation, i.e. the small number of constituents carrying the large fraction of momentum, the $p_\mathrm{T} D$ will be close to 1.

The girth and the momentum dispersion are related to the moments of the soi-disant generalized angularities defined as: $\lambda_\beta^\kappa = \sum_i (\frac{p_\mathrm{T,i}}{p_\mathrm{T,jet}})^\kappa (\frac{\Delta R_\mathrm{jet,i}}{R})^\beta$ [17]. For the number of jet constituents (κ, β) equals to $(0,0)$, the radial moment g corresponds to $(1,1)$ and for the square of the momentum dispersion $p_T D$ $(\kappa, \beta) = (2, 0)$. Only for $\kappa = 1$, the shapes are infrared and collinear (IRC) safe.

The difference of the leading track p_T ($p_\mathrm{T,track}^\mathrm{lead}$) and sub-leading track p_T ($p_\mathrm{T,track}^\mathrm{sublead}$) or *LeSub* is defined as:

$$LeSub = p_\mathrm{T,track}^\mathrm{lead} - p_\mathrm{T,track}^\mathrm{sublead}. \tag{2.4}$$

This shape is not an IRC-safe observable but shows toughness against contributions of soft background particles. An example of leading and sub-leading jets can be seen in Figure (2.6).

Figure (2.7) shows the measured jet shape distributions in 0–10% central Pb–Pb collisions at $\sqrt{s_\mathrm{NN}} = 2.76$ TeV for anti-k_T (see Subsection 4.2.2) charged jets at ALICE compared to JEWEL (see Chapter 5) simulation with and without recoils. As the resolution parameter is small, $R = 0.2$, the effects of medium recoils are also small. That means that the measurement is constrained by purely radiative aspects of the JEWEL shower modification. A good agreement between the data and the model, especially in momentum dispersion and *LeSub*, can be observed.
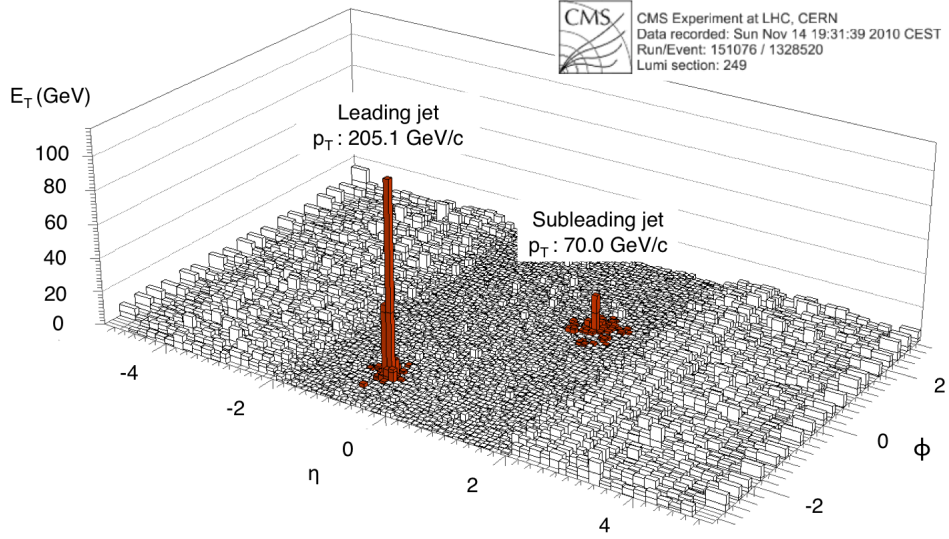
Figure 2.6: An example of jet pair in Pb+Pb collision at $\sqrt{s_{\mathrm{NN}}} = 2.76$ TeV [13].
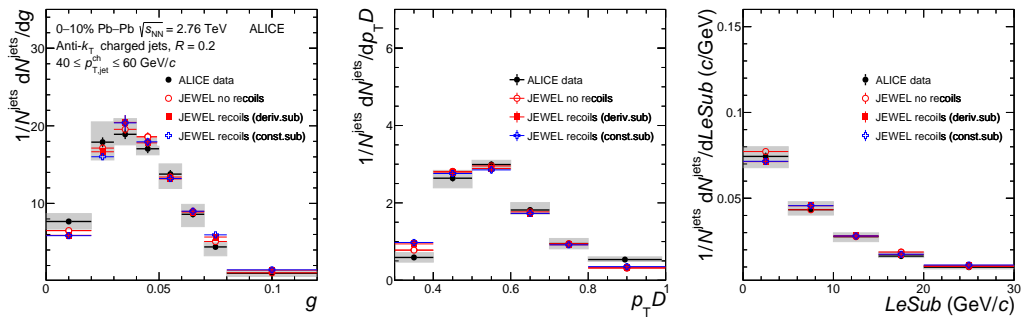

Figure 2.7: Jet shape distributions in 0–10% central Pb–Pb collisions at $\sqrt{s_{\mathrm{NN}}} = 2.76$ TeV for $R = 0.2$ in range of jet $p_{\mathrm{T,jet}}^{\mathrm{ch}}$ of 40–60 GeV/c compared to JEWEL with and without recoils with different subtraction methods. The colored boxes represent the experimental uncertainty on the jet shapes [18].

Chapter 3

RHIC and STAR

3.1 RHIC

The **R**elativistic **H**eavy **I**on **C**ollider (RHIC) is situated at Brookhaven National Laboratory. It is a long "chain" of different particle accelerators as can be seen from the Figure (3.1).
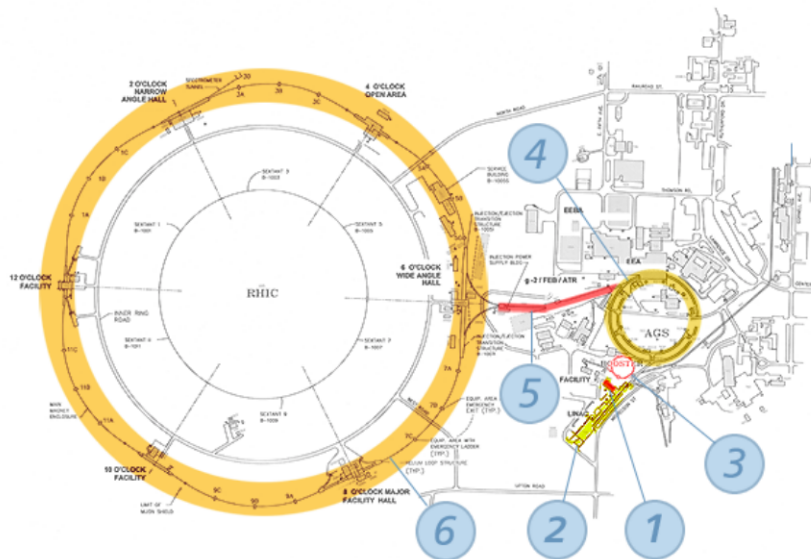

Figure 3.1: RHIC complex. 1 - Electron Beam Ion Source (EBIS), 2 - Linear Accelerator (Linac), 3 - Booster Synchrotron, 4 - Alternating Gradient Synchrotron, 5 - AGS-to-RHIC Line, 6 - RHIC [19].

Heavy ions start the movement from the Electron Beam Ion Source accelerator (1), which is a compact source and heavy ion accelerator. It serves as the start of the pre-injector system for RHIC and can create highly charged ion beams from almost any element. The ion beams are later accelerated in two small Linacs (2) and then carried to circular Booster synchrotron (3). The Booster provides the ions with more energy. Ions move forward with higher and higher speeds and then enter the Alternating Gradient Synchrotron (AGS) (4) at an approximately 37% speed of light. After the acceleration in the AGS the beam travels through the AGS-to-RHIC

Line (5) at 99.7% of the speed of light. At the end of this line a switching magnet sends the ion bunches down to one of the two beam lines, such that the bunches are directed right to the counter-clockwise RHIC direction and left to the clockwise RHIC direction. These beams are accelerated, as in the Booster Synchrotron or AGS, and then circulate in RHIC where they would collide in six interaction points. At four of the six interaction points a detector is located. They are PHOBOS (10 o'clock interaction point), BRAHMS (2 o'clock interaction point), STAR (6 o'clock interaction point) and sPHENIX, that will be at 8 o'clock interaction point. The first two experiments finished the data collection 11 years ago. Super PHENIX (sPHENIX) will be a new experiment that is proposed to replace the PHENIX experiment that was completed the last measurements in 2014.

3.2 STAR

The Solenoidal Tracker at RHIC (STAR) is an experiment that studies the formation and characteristics of QGP. It is designed to detect particles that arise as a result of the interaction of relativistic heavy ions or protons. The STAR detector system is shown in Figure (3.2). In central Au+Au collisions more than 1000 particles are formed. After the short-lived particles decay and the interaction of primary particles with the detector material the additional secondary particle fluxes arise. In order to identify each of these particles and to determine the trajectories, different types of calorimeters, detectors and counters are used.
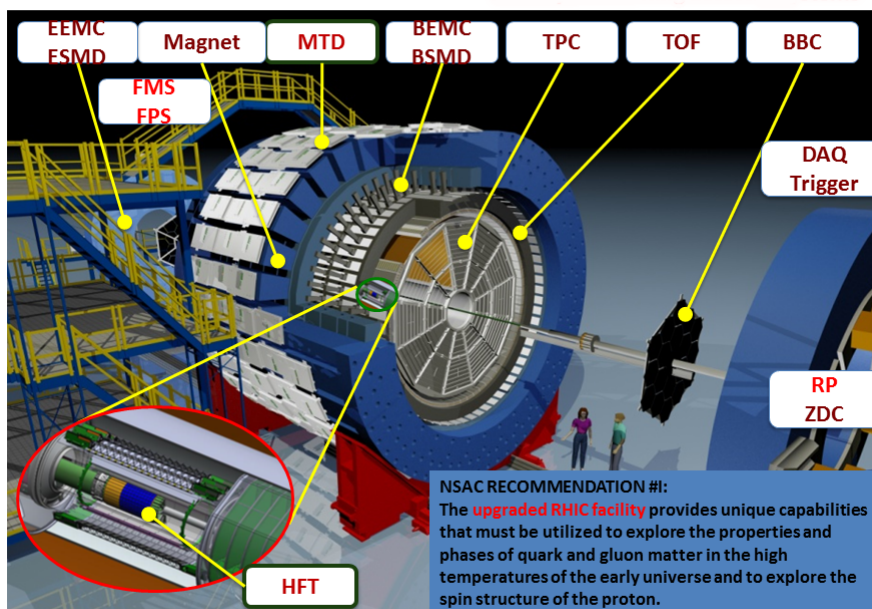

Figure 3.2: STAR detector system [20].

The **T**ime **P**rojection **C**hamber (TPC) is the main part of the system to measure charged particle tracks after collisions. The **B**arrel and **E**ndcap **E**lectro-**M**agnetic

Calorimeter (BEMC and EEMC) allow to measure hadronic and photonic energy deposition in the calorimeter towers. The **B**eam-**B**eam **C**ounter (BBC), **V**ertex **P**osition **D**etector (VPD) and **Z**ero-**D**egree **C**alorimeter (ZDC) are used to monitor collision luminosity and beam polarimetry. The **T**ime **O**f **F**light detector (TOF) of STAR is designed for improvement of direct identification of hadrons.

3.2.1 Time Projection Chamber

The TPC is the central part of the STAR detector system. It is a cylindrical detector with 4 m in diameter and 4.2 m in length built around the beam-line. The detector is filled with the gas in a well-defined, uniform, electric field of ≈ 135 V/cm. Electrically charged particles, that were produced in high-$\sqrt{s}$ heavy ion collisions, are deflected by the STAR magnet in a helical motion. The TPC is able to record those tracks, measure their momenta and identify particles by their ionization energy loss (dE/dx), which is calculated using the Bethe-Bloch formula [21]

$$-\frac{dE}{dx} = 4\pi N_A r_e^2 m_e c^2 z^2 \frac{Z}{A\beta^2} \left(\frac{1}{2} \ln \frac{2m_e c^2 \beta^2 \gamma^2 T_{max}}{I^2} \right) - \beta^2 - \frac{\delta}{2} - 2\frac{C}{Z}. \qquad (3.1)$$

Here, N_A is the Avogadro number, r_e is classical electron radius, m_e is the mass of the particle that losses energy, z is the charge of the incoming particle, ρ is material density, T_{max} is maximum energy transfer in a single collision, I is the mean excitation energy Z and A are the atomic number and nucleus weight respectively, δ and C are the density and shell corrections.

The TPC acceptance coverage is 2π in azimuthal angle ϕ and $-1.3 < \eta < +1.3$ in pseudorapidity. The TPC will be upgraded to inner TPC (iTPC). The upgrade
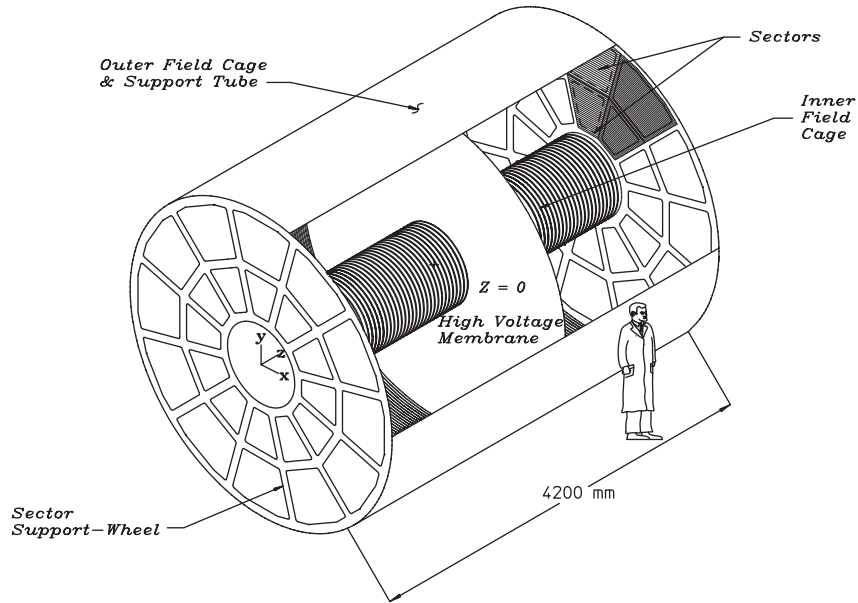

Figure 3.3: The layout of the STAR Time Projection Chamber [22].

17

will provide better momentum resolution and improved acceptance at high rapidity to $|\eta| < 1.7$. The layout of the STAR TPC is shown in Figure (3.3). It consists of a central membrane, an inner and outer field cage and two end-cap planes. The empty space between the central membrane and two end-caps is filled with P10 gas, which is 10% methane and 90% argon regulated at 2 mbar above atmospheric pressure. After the passage of the charged particles through the gas, the ionized secondary electrons drift toward the two end-caps in the uniform electric field which is provided by the two end-caps and the central membrane. The drifting electrons are then collected by the end-caps.

Figure (3.4) shows the track energy loss measured by the TPC in 2014 in 200 GeV Au+Au collisions with the different particle species associated to the observed bands.
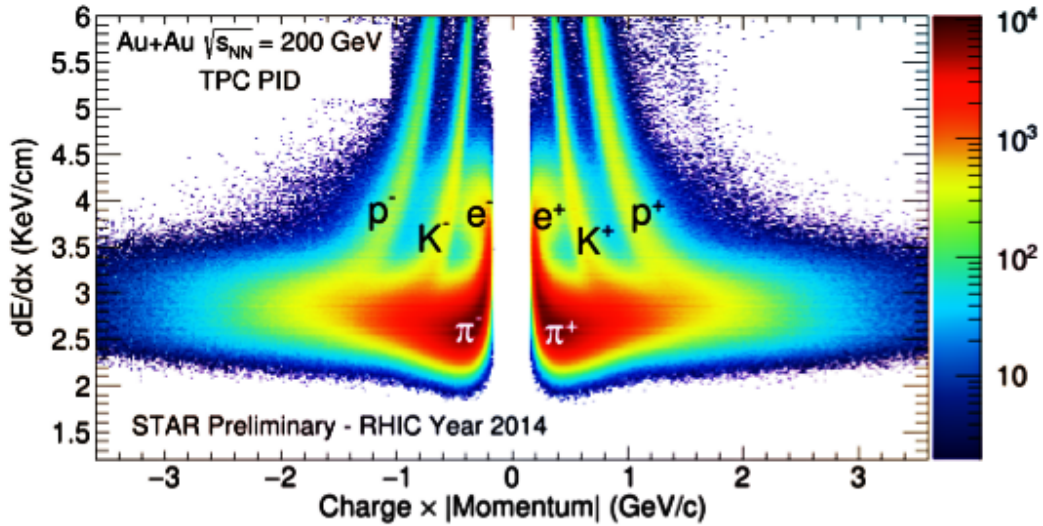

Figure 3.4: The energy loss measured in 200 GeV Au+Au collisions collected in 2014 at RHIC [23].

3.2.2 Barrel Electro-Magnetic Calorimeter

The Barrel Electro-Magnetic Calorimeter or BEMC is a lead-scintillator, sampling electromagnetic calorimeter. It surrounds the Central Trigger Barrel and the TPC. The BEMC allows STAR the triggering and studying of the high-p_T processes, e.g. jets, heavy quarks, due to its acceptance that is equal to that of the TPC for full length tracks (Figure (3.5)). The calorimeter coverage region is $-1 < \eta < 1$ in pseudorapidity and 2π in full azimuth. The neutral energy in the form of produced photons can be measured by detecting the particle cascade when those photons interact with the calorimeter. The calorimeter stack is stable in any orientation due to the friction between individual layers.

An end view of a module showing the mounting system and the compression components is shown in Figure (3.6).
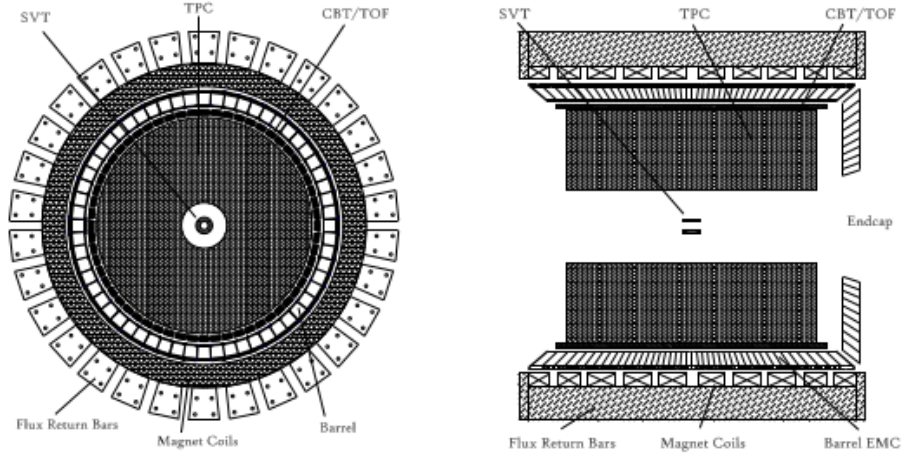
Figure 3.5: Cross sectional views of the STAR detector. The Barrel EMC covers $|\eta| \leq 1$. The BEMC modules slide in from the ends on rails which are held by aluminum hangers attached to the magnet iron between the magnet coils [24].
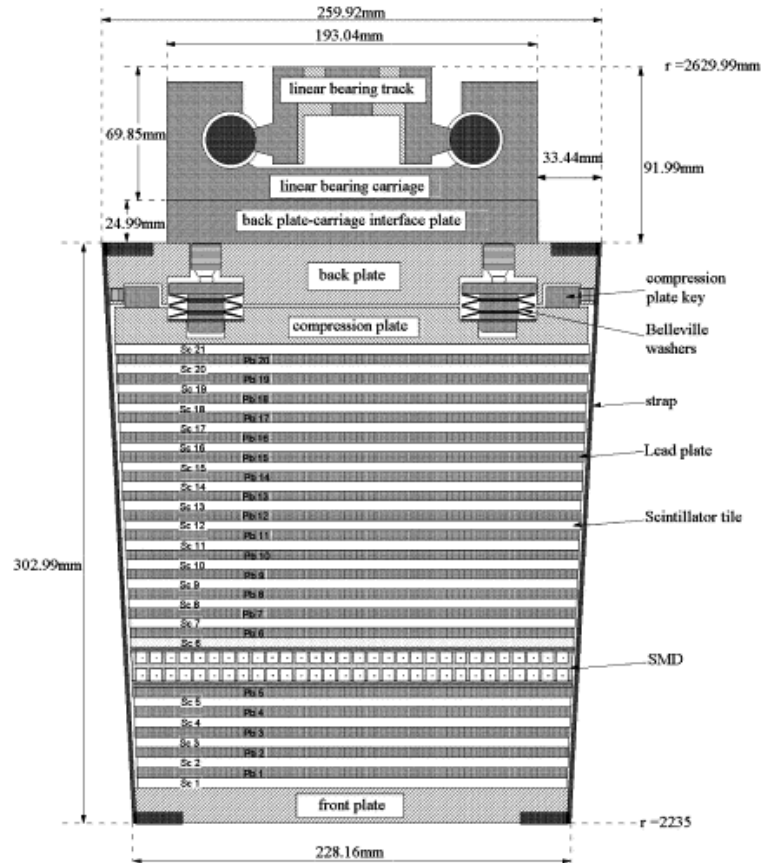

Figure 3.6: A side view of a STAR BEMC module. The image shows the location of the two layers of shower maximum detector at a depth of approximately 5 radiation length X_0 from the front face at $\eta = 0$ [24].

3.2.3 Endcap Electro-Magnetic Calorimeter

The Endcap Electro-Magnetic Calorimeter (EEMC) is a lead-scintillator sampling electromagnetic calorimeter that covers the west endcap of the Time Projection Chamber as it is depicted in Figure (3.7). There are 720 individual towers grouped together to provide coverage for pseudorapidity values $1 < \eta \leq 2$ and full azimuth range. The EEMC significantly enhances STAR's sensitivity to the flavor dependence of sea antiquark polarizations via $W\pm$ production in polarized p+p collision.
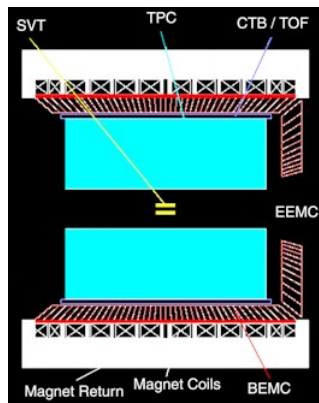

Figure 3.7: Endcap Electro-Magnetic Calorimeter [25].

3.2.4 Beam-Beam Counter

The Beam-Beam Counter or BBC is a set of scintillator rings installed around the RHIC beam pipe on the east and west pole tips of the STAR magnet. The schematic view of its positions is depicted in Figure (3.8).
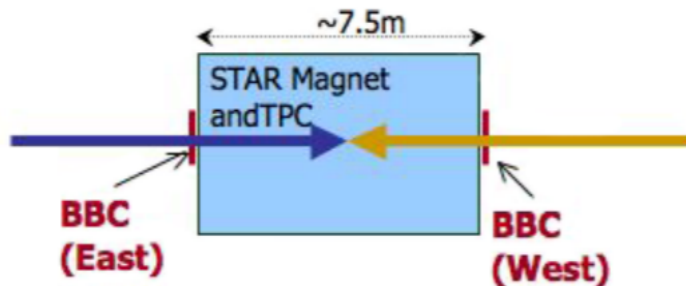

Figure 3.8: The schematic view of BBC positions. Blue and yellow arrows are the differently polarized proton beams [26].

Each counter consists of two rings of hexagonal scintillator tiles. An outer ring composed of large tiles and an inner ring composed of small tiles. Each of these annuli is internally divided into two separate subrings of 6 and 12 tiles each [25]. The primary vertex position will be determined by the timing difference between the two counters. The hexagonal tile annuli for BBC is depicted in Figure (3.9).
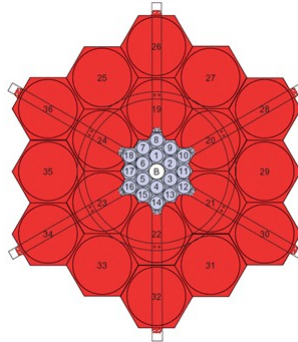
Figure 3.9: The Beam-Beam Counter [25].

3.2.5   Vertex Position Detector

The Vertex Positions Detector (VPD) provides the primary detector input to the STAR minimum bias trigger in Au+Au collisions. There are up to nineteen times measure by VPD in each event. These times are then used for the primary vertex along the beam pipe position Z_{vtx} calculation via

$$Z_{vtx} = c(T_{east} - T_{west})/2, \tag{3.2}$$

where c is the speed of light, T_{east} and T_{west} are the times from each of the two VPD assemblies. The times measured by the Vertex Position Detector are also needed for the start time T_{start} calculation as

$$T_{start} = (T_{east} + T_{west})/2 - L/c, \tag{3.3}$$

where L is the distance between the center of STAR and either assembly. The start time is lately used by the TOF to perform particle identification at mid-rapidity.
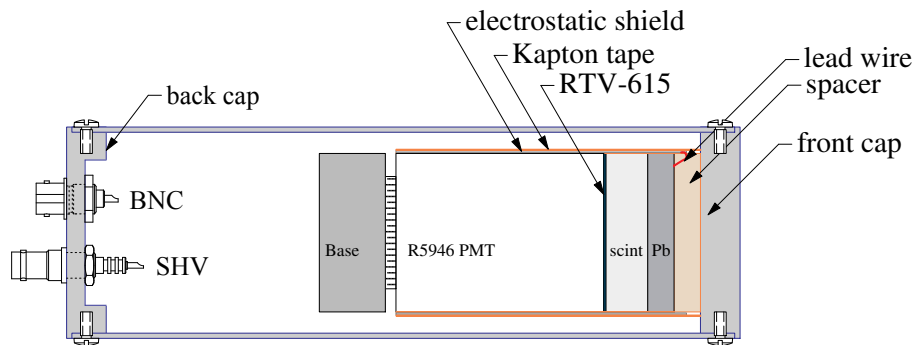

Figure 3.10: A schematic side view of Vertex Position Detector [27].

A schematic side view of VPD is shown in Figure (3.10). Each VPD assembly contain nineteen such detectors. Approximately half of the solid angle in the pseudorapidity range of $4.24 \leq \eta \leq 5.1$ is subtended by all of the nineteen detectors in each assembly.

3.2.6 Zero-Degree Calorimeter

The Zero-Degree Calorimeter (ZDC) is a small transverse area hadron calorimeter located downstream of the DX dipole magnets in STAR. This detector measures neutral energy within a 2 mrad cone about the beam direction. The detector is specially designed on the requirements of Au+Au runs. However, it is also used for the p+Au and p+p runs. The energy measurement in essence counts the number of free "spectator" neutrons that is lately use for the event-by-event characterization. The effective cross-section of the ZDC coincidence rate during the 200 GeV Au+Au collisions is approximately 10.4 barns [28].
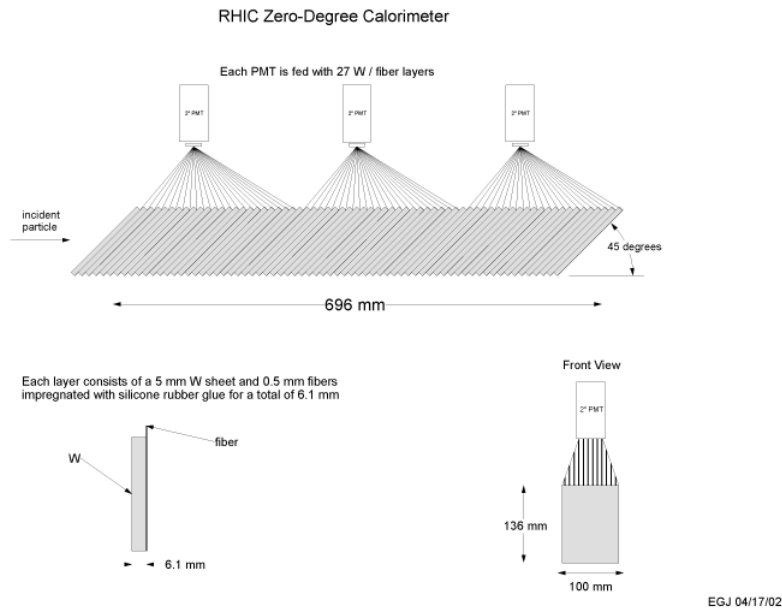

Figure 3.11: RHIC Zero-Degree Calorimeter [25].

The two ZDCs are located at the first bending magnets in the collider line. Each of the two calorimeters is split into three modules that consist of layers of lead in scintilator fibers going to a Photomultiplier (PMT) and Analog-to-Digital Converters (ADC). The determined number of spectator neutrons are then used as a minimum bias trigger.

3.2.7 Time Of Flight

As it can be seen for the Figure (3.12) the Time Of Flight (TOF) system is located around the Time Projection Chamber. The TOF measures time intervals with a specific precisions. While the VPD measures the "start time" of the particle, the TOF measures the so-called stop time of the particle. The difference, Δt, between these times is the time of flight of the particle. Using the data from the TPC the
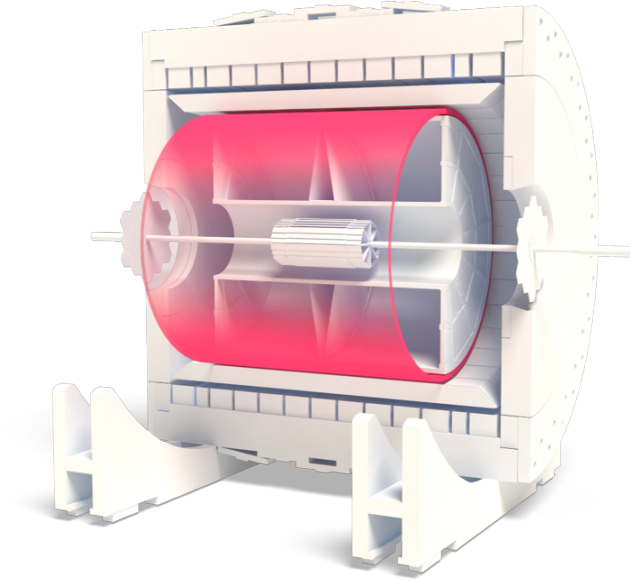
Figure 3.12: The TOF system [25].

inverse velocity $1/\beta$ for each track and the particle mass M can be calculated as

$$\frac{1}{\beta} = c\frac{\Delta t}{s}, \tag{3.4}$$

$$M = p\sqrt{\frac{1}{\beta^2} - 1}, \tag{3.5}$$

where s is the total path length, p is the momentum and c is the speed of light.
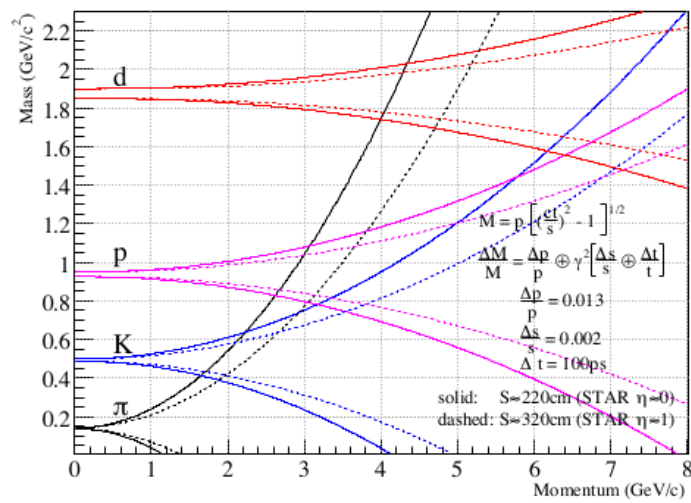

Figure 3.13: The momentum dependence of the particle mass resolution for a 100 ps time resolution for pions, kaons, protons and deuterons [29].
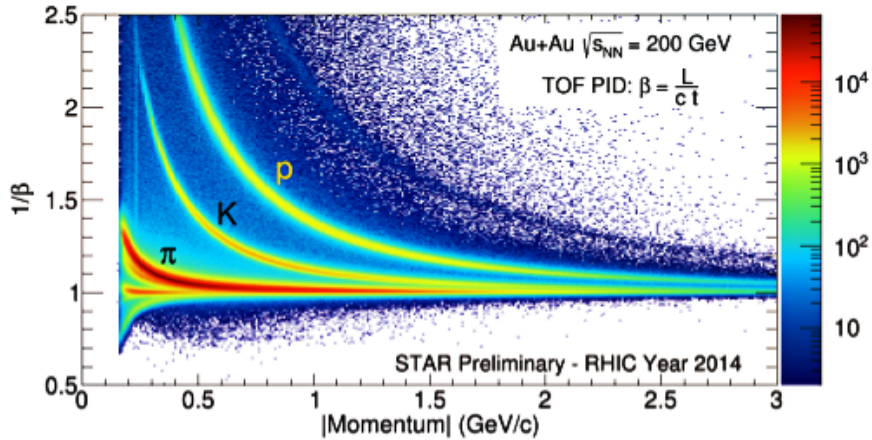
Figure 3.14: TOF particle identification from $1/\beta$ measured in 200 GeV Au+Au collisions collected in 2014 at RHIC [23].

The momentum dependence of the particle mass resolution for a 100 ps time resolution for pions, kaons, deuterons and protons is shown in Figure (3.13). The upper line in the pair shows the dependence of $M + \Delta M$ versus the momentum. The $M - \Delta M$ dependence on the momentum is demonstrated by the lower line. An example of particle identification with the TOF from 2014 Au+Au collisions at the top RHIC energy is shown in Figure (3.14). It can also be seen from this figure that with the increasing momentum pions are the first particles leading to a significant background in the proton identification and the first background to deuteron identification.

The TOF system can provide direct K, p or π identification up to momenta $p \sim$ 1.7 GeV/c, proton identification up to $p \sim 2.6$ GeV/c, deuteron identification out to $p \sim 4$ GeV/c [29].

3.2.8 Heavy Flavor Tracker

The Heavy Flavor Tracker or HFT which is depicted in the Figure (3.15) is a new tracker of STAR installed in the 2014 and removed in 2016 after reaching very successfully its goals. The HFT enables precision tracking measurements of heavy quarks, like B^0 or D^0, at low momentum where the particle production is most sensitive to the bulk medium created in heavy ion collisions. This allows to distinguish the decay vertices of heavy flavor particles from primary vertices and significantly reduces combinational background, which yields cleaner measurements with a higher level of significance.

There are three detectors that component the Heavy Flavor Tracker: a silicon pixel detector (PXL), a double-sided Silicon Strip detector (SSD) and an Intermediate Silicon Tracker (IST). The HFT structure is shown in Figure (3.16). Since the minimal radius of the HFT is only 2.5 cm, it tightly surrounds the beam pipe. The SPD and the IST lie inside the radial location of the SSD. The Intermediate Silicon
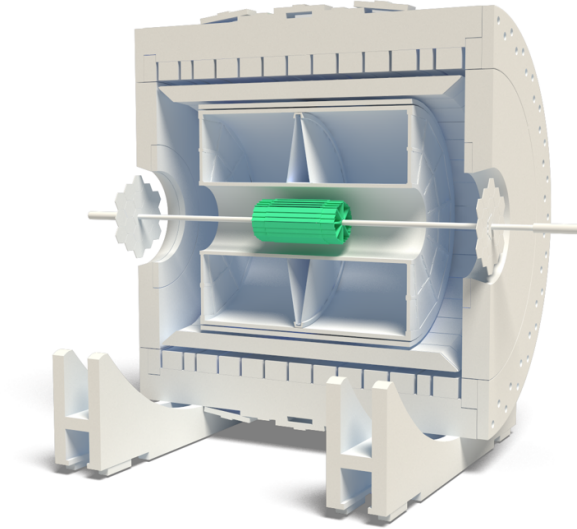
Figure 3.15: The Heavy Flavor Tracker [25].

Tracker is a single-sided double-metal silicon pad that matches the high resolution of the PXL with the high resolution of the Time Projection Chamber and the SSD. The IST is composed of two layers. The inner layer lies at a radius of 12 cm and consists of 19 ladders of 40 cm length [30]. The outer layer lies at a radius of 17 cm and consists of 27 ladders of 52 cm length. The strips on the inner layer are oriented to give the best resolution in the $r - \phi$ direction, while the strips of outer layer are oriented to give the best resolution in z direction.
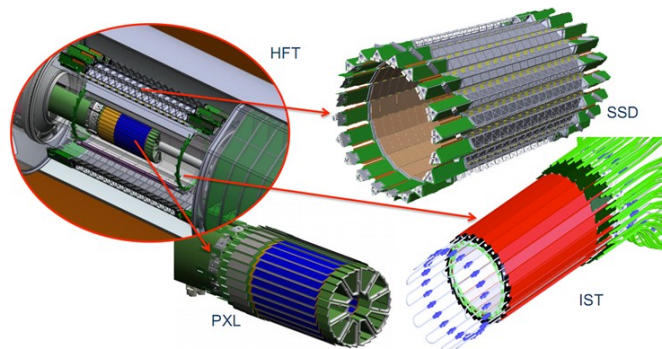
Figure 3.16: The Heavy Flavor Tracker parts. PXL - Pixel Detector, IST - Intermediate Silicon Tracker, SSD - double-sided Silicon Strip Detector [25].

The HFT Pixel Detector is the first operational vertex detector based on Monolithic Active Pixel Sensors (MAPS) or also called CMOS Pixel Sensors (CPS). It is a low mass detector located close to the beam pipe. For this reason, the Pixel Detector achieves the maximum resolution. As the IST, the PXL is also composed of two layers. The inner layer is located at a radius of 2.5 average radius and has 9 ladders. The outer one is located at a 7 cm radius and consists of 24 ladders.

Chapter 4

Algorithms of jet reconstruction

4.1 Attributes of the ideal algorithm

In order to reconstruct jets different algorithms are used. There are four criteria that an ideal jet algorithm is desirable to have.

1. The algorithm should be infrared and collinear (IRC) safe and also find jets that are insensitive to any soft and collinear radiation in the event.

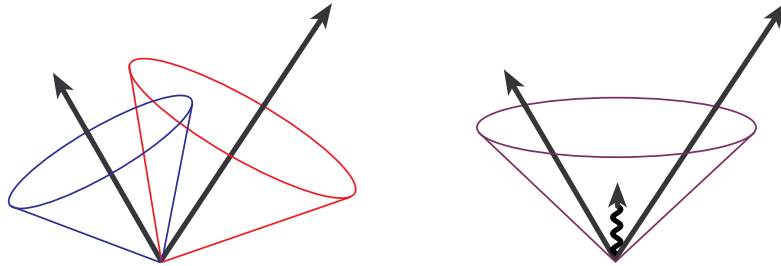Figure 4.1: An example of infrared sensitivity in cone jet clustering. Seed particles are shown as arrows with the length proportional to energy [31].

Figure (4.1) illustrates an infrared sensitivity in cone jet clustering. It is seen that jet clustering begins around seed particles. The soft radiation should not affect jet configuration.
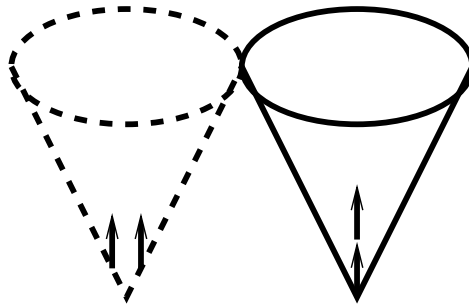

Figure 4.2: Collinear sensitivity in jet reconstruction [31].

In Figure (4.2) the collinear sensitivity in jet reconstruction can be observed. The right cone produces a seed due to the more narrowly distributed energy, while the left one cannot produce a seed as energy splits among several detector towers.

2. Jet finder should be fully specified. Therefore, all parts of the algorithm, such as merging, splitting, clustering, energy and angle definition, etc., and all the algorithmic processes should be clearly and completely described.

3. After jets enter a detector, different effects, such as particle showering, noise, detector response, etc., will to some extent influence the performance of even the most ideal jet algorithm. For this reason the algorithm should not depend on the cell type, number or size of detector.

4. As the jet finding algorithm should be equal at all levels, the same jets should be found at the parton, particle and detector level.

5. The algorithms should be also easy to implement in perturbative calculations, with typical experimental detectors and data.

6. The jet algorithm should use the computer resources efficiently. So, the jet identification should be provided with a minimum of computer time.

All jet finding algorithms can be divided in two types: cone jet algorithms and sequential-clustering algorithms. *Cone jet finding algorithms* are based on identifying energy-flow into cones in pseudorapidity $\eta = -\ln \tan \frac{\theta}{2}$ and azimuth ϕ (see Appendix A). *Sequential-clustering jet algorithms* are based on successive pair-wise recombination of particles. These algorithms are infrared safe. As the cone jet algorithms are not so effective and also violate the IRC safety, this thesis will be focused on sequential-clustering jet finding algorithms.

4.2 Sequential-clustering jet algorithms

The difference between the sequential recombination and cone methods is in their sensitivity to non-perturbative effects like hadronization and underlying event (UE) contamination.

All the sequential-clustering jet finding algorithms are defined as follows. Firstly, the algorithm finds the distance, d_{ij}, between particles i and j as

$$d_{ij} = \min(k_{ti}^{2p}, k_{tj}^{2p}) \frac{\Delta_{ij}^2}{R^2}. \tag{4.1}$$

$\Delta_{ij}^2 = (y_i - y_j)^2 + (\phi_i - \phi_j)^2$ and k_{ti} or k_{tj}, y_i, ϕ_i and R stand for the transverse momenta, rapidity, azimuth and radius parameter of particle i respectively. A parameter p controls the relative power of the energy versus geometrical (Δ_{ij}) scales.

Secondly, the algorithm calculates the distance, d_{iB} between the entity i and the beam B as

$$d_{iB} = k_{ti}^{2p}. \tag{4.2}$$

The next step of the clustering jet algorithm is to find the minimum distance, d_{min} between the distances d_{ij} and d_{iB}. In case the smallest distance is d_{ij}, the

algorithm provides a recombination of the entities. In other situation, i is called to be a jet and is subsequently removed from the list. All these steps are repeated until no particles are left.

Depending on the parameter p, the sequential-clustering jet finding algorithms can be divided into 3 types: kT ($p = 1$), anti-kT ($p = $ -1) and Cambridge/Aachen ($p = 0$) algorithms. As the Cambridge/Aachen is not used in the analysis, the first two algorithms will be described below.

4.2.1 kT jet algorithm

The kT jet algorithm is defined by the equations 4.1 and 4.2 with $p = 1$. After the algorithm finds the minimum distance d_{min}, the following situations could occur:

- $d_{min} = d_{ij}$. In this case the particles are merged summing their four-momenta.

- $d_{min} = d_{iB}$. A particle is called to be a final jet and is afterward removed form the list.

One of the advantages of the kT algorithm is that it explicitly imitates the a walk through the QCD branching sequence. As the the largest part of the particles radiated from an original hard parton is clustered in the reconstructed jet, better particle mass measurements, general kinematic reconstruction and gaps-between-jets identification could be obtained. Another benefit of this algorithm is the disintegration of jet into constituent subjets, that can be useful for identifying decay products of fast-moving heavy particles. However, the kT jet algorithm has also its disadvantages. The main problem of the algorithm was originally its slowness. Clustering N particles into jets requires $\mathcal{O}(N^3)$ operations. However, this problem has been already solved (see Section 4.3). As the kT algorithm is sensitive to the background in comparison to other algorithms, it is mostly used for the background estimation.

4.2.2 Anti-kT jet algorithm

The anti-kT jet algorithm is defined by the equations 4.1 and 4.2 with $p = $ -1. Unlike the kT jet-finder, the anti-kT algorithm firstly finds the hardest particle (having the largest p_T). In the next step, the algorithm finds the minimum distance between this hard particle and the remaining soft ones. The minimum distances are defined just by the transverse momentum of the particle having the highest p_T and the distance Δ_{1i} between the first ("1") and other hard particles (i). The shape of the jet is determined only by the distance between the two hard particles as the soft particle do not modify the jet shape. Overall, three cases are distinguished:

1. There are no other hard particles within the distance $2R$ from the given hard particle. Such a hard particle will collect all the soft particles around itself inside a radius R. As a result a perfect conical jet will be acquired.

2. The second hard particle is located within a distance $R < \Delta_{12} < 2R$. As a result, two hard jets will be obtained. The only difference will be in the shapes of these jets. Depending on the particle transverse momenta (k_{t1} and k_{t2}) the following three cases could be distinguished:

- $k_{t1} \gg k_{t2}$: in this situation the first jet will have a conical shape, while the second jet will be partly conical since it will miss the part crossing the first jet (see the light-blue jet depicted in the Figure (4.3) right).

- $k_{t1} = k_{t2}$: none of the jets will have a conical shape, the overlying area will be divided into two equal parts (compare the blue and the gray jets shown in the Figure (4.3) right).

- $k_{t1} \sim k_{t2}$: both cones will be clipped. The boundary b between them will be defined as $\Delta R_{1b}/k_{t1} = \Delta_{2b}/t_{t2}$.

3. The second hard particle is within a distance $\Delta_{12} < R$. As a result, the two particles will cluster to form a single jet. Likewise the previous case, the shape of the jet will depend on the hard particles transverse momenta and can be thereby divided into two situations:

- $k_{t1} \gg k_{t2}$: there will be a conical jet centered on k_{t1}.

- $k_{t1} \sim k_{t2}$: the shape of the jet will be a union of cones having the radius R around each hard particle plus a cone of radius R centered o the final jet.
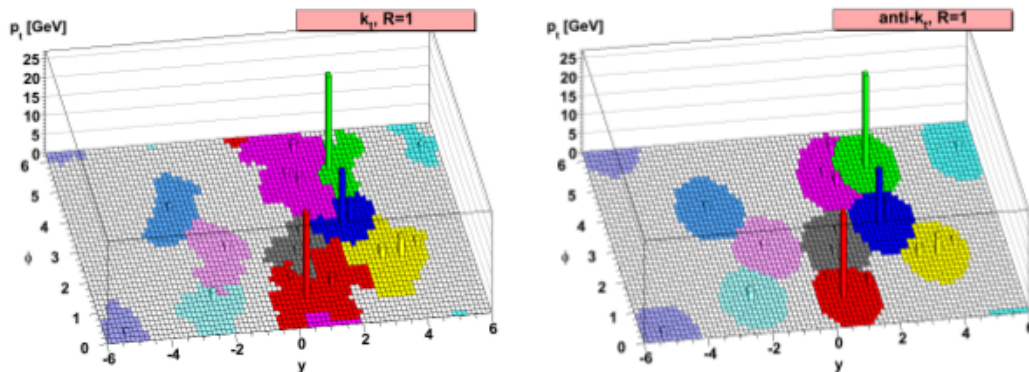

Figure 4.3: A sample parton-level event generated with HERWIG Monte-Carlo generator of p+p collision clustered with kT and anti-kT algorithms [32].

A comparison of the kT and anti-kT algorithm behavior is shown in Figure (4.3). A parton-level event was taken together with 10^4 soft particles and then clustered with the kT and the anti-kT algorithm respectively. It can be seen, that for the kT algorithm there are irregular shapes of jets, while the anti-kT algorithm gives jets the regular shape as described in the item 2.

Area related properties

In order to discuss the properties of jet boundaries for different algorithms, the calculations of jet areas are used. The jet areas can be active or passive. The active jet area measures jet susceptibility to diffuse radiation and is defined as

$$A(J|\{g_i\}) = \frac{\mathcal{N}_g(J)}{\nu_g},\qquad(4.3)$$

where ν_g is the number of ghosts per unit area and $\mathcal{N}_g(J)$ is the number of ghosts contained in the jet J and $\{g_i\}$ is the given specific set of ghosts [33]. An example of such an area can be seen in the left part of Figure (4.3).

Passive area measures jet susceptibility to point-like radiation and can be calculated using the following equation:

$$a(J) \equiv \int dy\, d\phi\ f(g(y, \phi), J) \qquad f(g, J) = \left\{ \begin{array}{ll} 1 & g \in J \\ 0 & g \notin J \end{array} \right. . \qquad (4.4)$$

That corresponds to the 4-vector area of the region where g is clustered with J

$$a_\mu(J) \equiv \int dy\, d\phi\ f_\mu(g(y, \phi), J) \qquad f_\mu(g, J) = \left\{ \begin{array}{ll} g_\mu/g_t & g \in J \\ 0 & g \notin J \end{array} \right. , \qquad (4.5)$$

where g_t is the ghost transverse momentum. In case of a jet with small area $a(J)$, the 4-vector area has the properties that its transverse component satisfies $a_t(J)$ $= a(J)$. The area is also approximately massless and points in the direction of J. Otherwise, when the area of jet $a(J) \sim 1$, the 4-vector area receives a mass and may not point in the same direction as J. For the typical IRC safe algorithm it is also important to note that jet passive area equals πR^2 only when $\Delta_{12} = 0$. Increasing Δ_{12} changes the area.
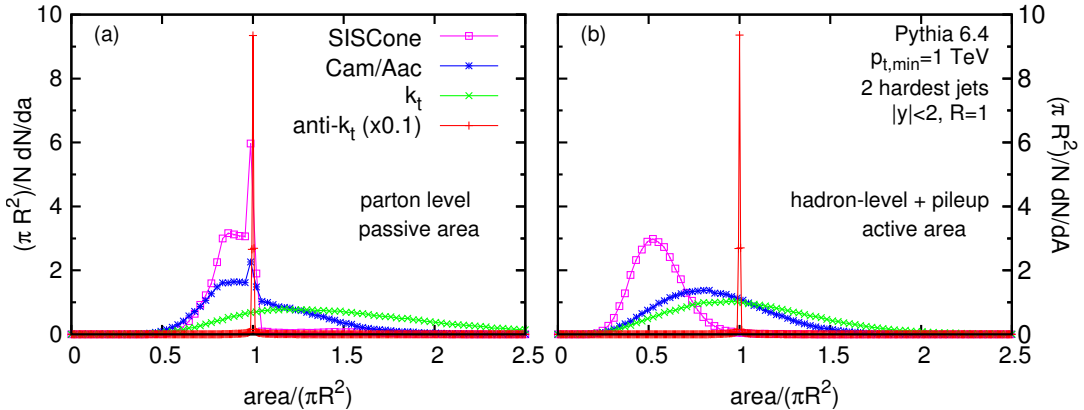

Figure 4.4: Distribution of areas in di-jet events at the LHC for various jet finding algorithms. The events were generated by PYTHIA 6.4. (a) passive area at parton level, (b) active area at hadron level including UE and pile-up [32].

In Figure (4.4) the distributions of passive (left) and active (right) areas at parton and hadron levels respectively in di-jet events at the LHC can be observed. The distributions are calculated for cone jet algorithm SISCone [34] and three different clustering jet algorithms (Cambridge/Aachen, kT and anti-kT) using the PYTHIA 6.4 Monte-Carlo generator.

4.3 FastJet

FastJet is a software package [32] , [35], [36] containing most of jet finding algorithms. Besides, this different tools for jet area calculation and background subtraction
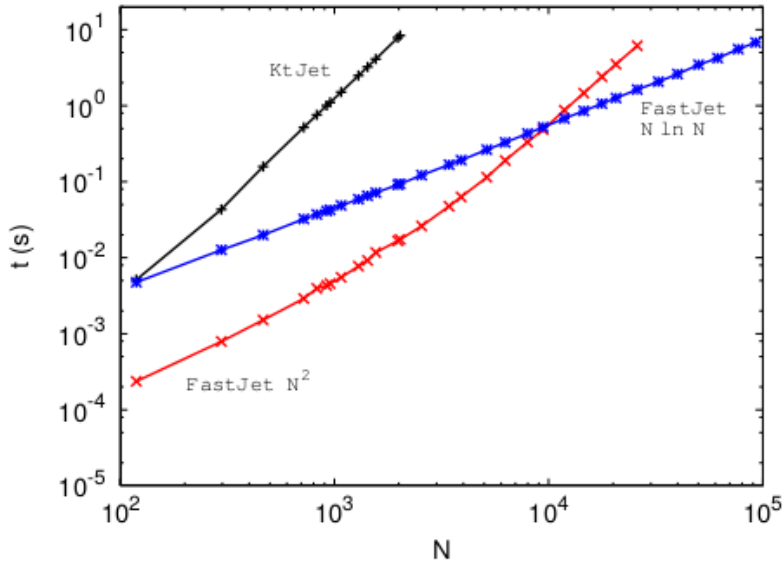
Figure 4.5: The running times of kT jet-finder and FastJet implementations of the kT clustering algorithm versus the number of initial particles [36].

performance needed for various jet related analysis are also implemented in the package.

As it was discussed before, one of the main disadvantages of the kT algorithm used to be originally its slowness. This problem was solved in the implementation of the kT jet-finder in the FastJet. Through the use of Voronoi diagrams and a Delaunay triangulation for identification of the each particles geometrical nearest neighbor, the geometrical aspects of the problem are isolated. The FastJet implementation, therefore, reduces the kT algorithm complexity from N^3 to $N \ln N$ operations. Concerning this, the kT jet-finder can be used for large values of N that rise when considering all cells of a finely segmented calorimeter and for heavy-ion events. A comparison of the running times of kT jet finding algorithm and its FastJet implementation is depicted in Figure (4.5). It can be clearly seen that during the same time the FastJet will cluster larger number of particles.

Chapter 5

JEWEL

Jet **E**volution **W**ith **E**nergy **L**oss (JEWEL) is a Monte Carlo (MC) event generator that describes the QCD evolution of jets in vacuum and in a medium in a perturbative approach [37], [38], [39]. Since JEWEL simulates only jets, the UE in p-p and the remaining events in nucleus-nucleus collisions are not included. A fully microscopic description of jet interpretation in a medium including coherence effects in implemented in JEWEL makes it quite complex.

5.1 Physics of JEWEL

There are four assumptions on which JEWEL MC generator is based. Firstly, the medium resolved by the jet should consist of a collection of quasi-free partons. Secondly, there is an ability of usage an infrared continued version of the perturbative scattering matrix elements in order to describe all interactions of jets in medium. In JEWEL the interplay of different sources of radiation is governed by the formation times. Due to the generalization of the probabilistic formulation in the eikonal limit to general kinematics the Landau-Pomeranchuk-Migdal, or LPM, effect (see Appendix B) is included as well. Therefore, JEWEL uses the LO matrix elements not only for the initial production of hard jets, but also for the rescattering of jets off partonic constituents of the medium.
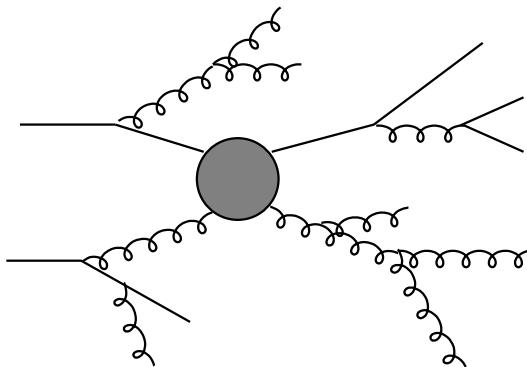

Figure 5.1: Schematic picture of extra emissions generated by the parton shower on top of a hard quark-gluon scattering effect described by a $2 \rightarrow 2$ matrix element [37].
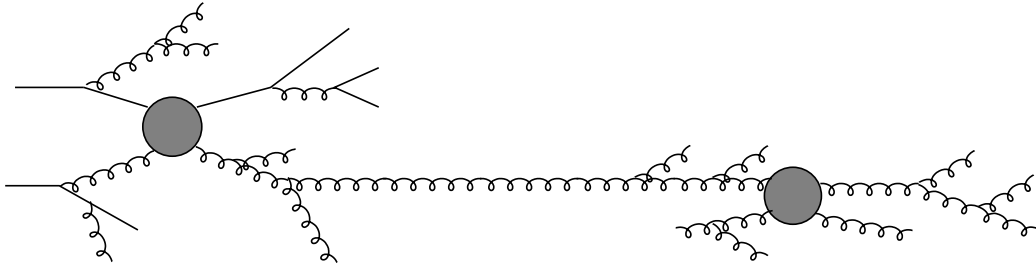
Figure 5.2: Schematic picture of extra emissions in two well separated events. The re-scattering is only indicated for one parton [37].

The hard scattering process in QCD is described by the matrix elements at fixed order in perturbation theory. It is important to consider only $2 \longrightarrow 2$ processes, because they are the lowest order scattering processes. However, as the radiative corrections can be large, it is extremely important always to take them into account. Versatility and simple structure of the leading contribution of radiative corrections allows systematically to construct approximations for the full higher order ($2 \longrightarrow 3$, $2 \longrightarrow 4$, etc.) matrix elements. For this aim, in MC generators a hard scattering configuration from the $2 \longrightarrow 2$ matrix elements is generated first, then the leading radiative corrections with a parton shower, attaching extra emissions to all incoming and outgoing legs of the hard scattering, are added. Figure (5.1) shows an example of a hard quark-gluon scattering event (shaded circle).

Besides that the parton shower is unitary, it also resums the leading logarithmic contributions to all orders. The extra emissions are ordered in a variable that characterizes their hardness. As in the IR region the probability for gluon emission diverges, the parton shower has to be cut off at a suitable scale. Otherwise, a very soft or very collinear emissions will always end up in the same hadron as the emitting parton and therefore will not be observable.

Figure (5.2) shows the so-called on-shell parton rescattering in a medium. That means that there is a large distance as well as between subsequent re-scatters in comparison to the time required for the parton shower evolution. As the the parton shower of the initial hard scattering producing the event has not terminated by the time of the re-scattering, there may be several emissions happening at the same time. In that case, the emission with shorter formation time gets formed as a parton while the others are discarded as it is depicted in Figure (5.3).
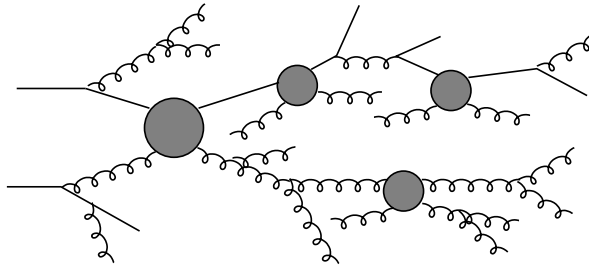

Figure 5.3: Schematic picture of extra emissions and re-scatters taking place on comparable time scales [37].

5.2 A simple model of the medium

Working with a simple model of a medium, one can understand which features in the data can be accounted for by microscopic dynamics. In order to connect centrality to impact parameter b and to compute the density of binary nucleon-nucleon collisions $n_{coll}(b;\ x,\ y)$ and number of participants $n_{part}(b;\ x,\ y)$ in the transverse plane a Glauber model (see Section 1.4) is used. Consider the initial di-jet production taking place at $t = z = 0$, then $n_{coll}(b;x,y)$ gives the distribution in transverse plane. There are two parameters determining the hydrodynamic evolution of the system. The first is the initial temperature T_i in the center ($x = y = 0$) of a central collision. The second one is the time τ_i suitable for the start of the evolution. Assumptions of having a symmetric A+A collision and that the initial energy density $\epsilon(b;x,y,\tau_i)$ is proportional to the density of participants

$$\epsilon(b;x,y,\tau_i) = \epsilon_i \frac{n_{part}(b;x,y)}{\langle n_{part}\rangle(b=0)} \quad \text{with} \quad \langle n_{part}\rangle(b=0) \approx \frac{2A}{\pi R_A}, \qquad (5.1)$$

fix the transverse profile. The R_A stands for the radius of the nucleus and $\epsilon_i \propto T_i^4$ is related to the initial temperature. The whole centrality dependence is determined by the Equation (5.1).

As the jet evolution is characterized by the high scales set by the initial jet production, the jets are protected from disturbances due to re-scattering in the
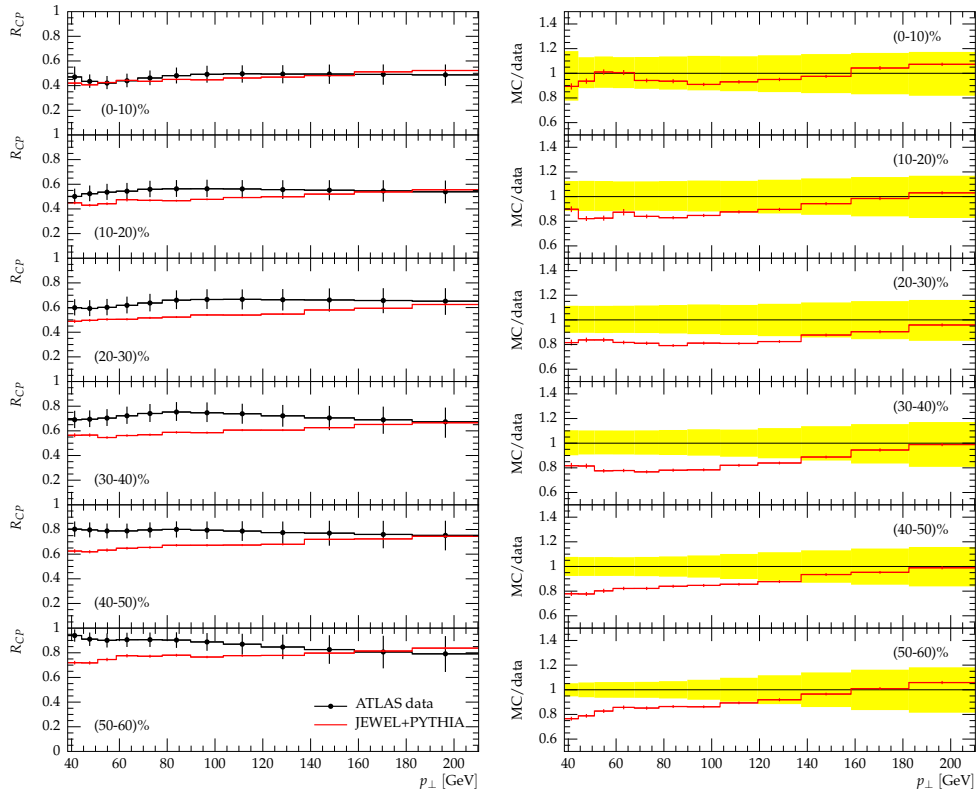

Figure 5.4: Centrality dependence of the jet nuclear modification factor R_{CP} for $R = 0.2$ and $|\eta_{\text{jet}}| < 2.1$ [38].

medium. Due to this JEWEL has low sensitivity to the assumptions about the very early phase of the medium. In JEWEL solely the deconfined phase is examined. Considering this, rescattering is only possible as long as the local temperature has higher values than the critical temperature T_c.

An example of using JEWEL in practice is demonstrated in Figure (5.4). Here, the centrality dependence of the nuclear modification factor R_{CP} in Pb–Pb collisions at $\sqrt{s_{NN}} = 2.76$ TeV measured by the ATLAS Collaboration is shown for a jet having the resolution parameter $R = 0.2$. A reasonable agreement between JEWEL and ATLAS data can be seen in the most central bin. Other bins have the similar shape, but show slightly worse results.

5.3 Simulation in JEWEL

In this section the simulation in JEWEL will be described. For this thesis 50 million events were simulated for the interaction in vacuum and 20 million events for the interaction in medium. The simulation was made for 0–10% central and 60–80% peripheral "recoils on/off" collisions. Table 5.1 contains the parameters used for the vacuum model. Additional parameters for the simulation with medium can be found in the Table 5.2.

Name of parameter	Name in JEWEL	Value	
		Central	Peripheral
Parton Distribution Function set	PDFSET	10100	
Number of events	NEVENT	100000	
Mass number of Au nucleus	MASS	197	
The CMS energy of the colliding system	SQRTS, [GeV]	200	
Minimum p_T in matrix element	PTMIN, [GeV]	3	
Maximum p_T in matrix element	PTMAX, [GeV]	-1	
The switch of keeping recoils	KEEPRECOLIS	T	F
The rapidity range	ETAMAX	2.5	

Table 5.1: Parameters of the JEWEL vacuum simulation for central and peripheral "recoils on/off" collisions. [37].

The size of jet is quantified by resolution parameter R. For this thesis values of the resolution parameter were chosen to be $R = 0.2$ and $R = 0.4$ respectively. The charged particles were simulated in pseudorapidity $\eta_{cent} = 2.5$ and full azimuth. All particles were required to have the CMS energy $\sqrt{s_{NN}} = 200$ GeV. Jets were reconstructed with the anti-k_T algorithm included in FastJet software package (see Section 4.3 and Subsection 4.2.2). The results of the simulation are presented in Chapter 6.

Name of parameter	Name in JEWEL	Value	
		Central	Perihperal
The initial (mean) temperature	TI, [GeV]	0.28	
The initial time τ_i	TAUI, [fm]	0.6	
An integer mass number of colliding nuclei	A	197	
The lower end of centrality range	CENTRMIN, [%]	0	60
The upper end of centrality range	CENTRMAX, [%]	10	80
The nucleus-nucleus cross-section	SIGMANN, [fm^2]	4.2	

Table 5.2: Parameters of the JEWEL simulation with medium for central and peripheral "recoils on/off" collisions [37].

Chapter 6

Results of analysis

In this chapter the results of jet shape analysis in JEWEL are presented. The analysis is performed for Au+Au central and peripheral collisions at $\sqrt{s_{\mathrm{NN}}} = 200$ GeV with "recoils on/off" option. The radial moment g, momentum dispersion $p_T D$ and $LeSub$ are calculated for different values of the resolution parameter R and jet p_T for medium "recoils on/off" and vacuum simulation separately.
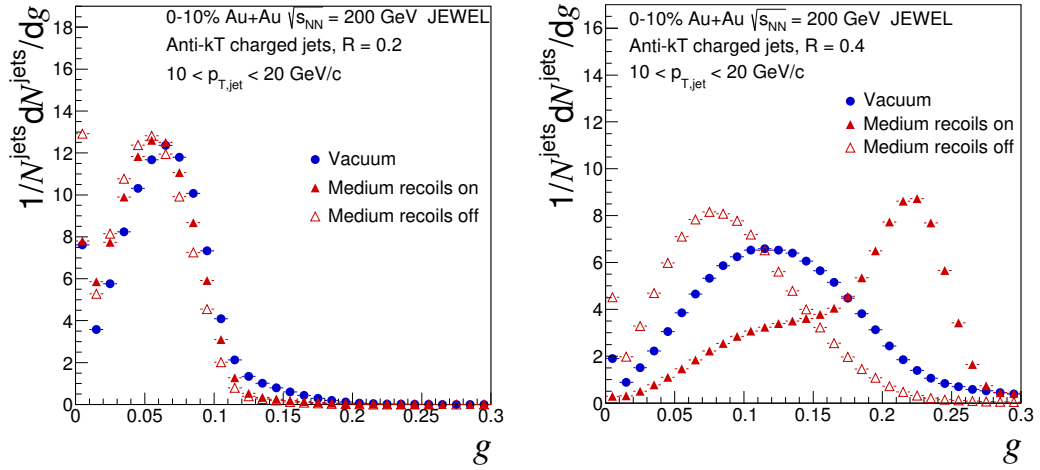
6.1   Angularity

Figure 6.1: Angularity for central Au+Au collisions at $\sqrt{s_{\mathrm{NN}}} = 200$ GeV. $R = 0.2$ (left) and $R = 0.4$ (right) in $10 < p_T < 20$ GeV/c.

The angularity was calculated by the Equation (2.2). Figures (6.1) and (6.2) compare the radial moment for vacuum and medium "recoils on/off" central Au+Au collisions in two different p_T ranges $10 < p_T < 20$ GeV/c and $20 < p_T < 30$ GeV/c respectively. Figures (6.3) and (6.4) compare the angularity for vacuum and medium "recoils on/off" peripheral Au+Au collisions in the same p_T ranges. As it can be seen, the angularity has the same behavior for $R = 0.2$. Nevertheless, peaks for the medium "recoils on" and medium "recoils off" simulation of radial moments with $R = 0.4$ are shifted to the right and left respectively. Distributions for medium

"recoils on" collisions with $R = 0.4$ have longer tail than others. Also, the spike for $g = 0.01$ in $10 < p_T < 20$ GeV/c can be observed for both resolution parameters. That signals of the presence of jets with only one constituent. In order to probe this, the dependence of the number of constituents on the angularity is in Figure (6.5). It can be clearly seen that there is a larger amount of particles for $R = 0.4$ than for $R = 0.2$ jets. Figure (6.6) compares number of entries for different numbers of constituents in medium "recoils on" central collisions. Statistical results for central "recoils off" and peripheral "recoils on/off" collisions could be found in Appendix C. We would like to note that all the results were obtained without any background subtraction. For this reason, such a difference in the position of peaks can be observed.
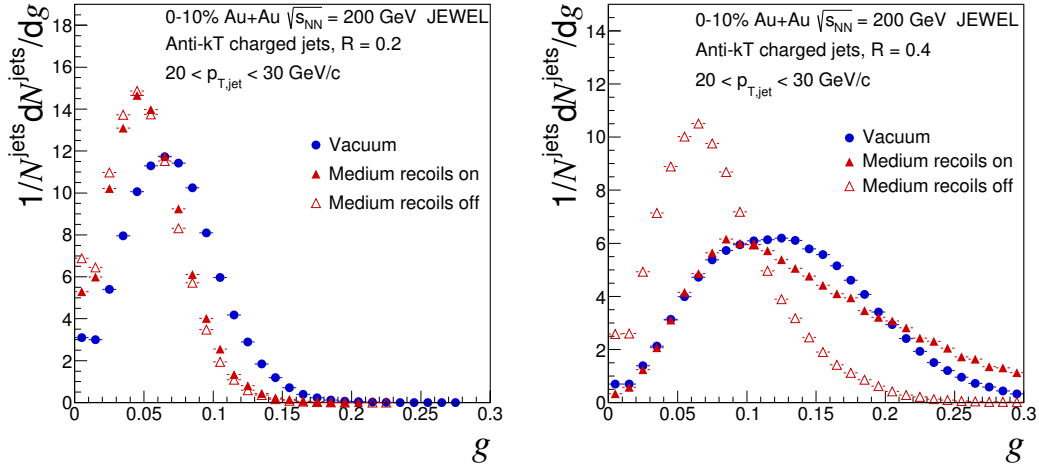

Figure 6.2: Angularity for central Au+Au collisions at $\sqrt{s_{\mathrm{NN}}} = 200$ GeV. $R = 0.2$ (left) and $R = 0.4$ (right) in $20 < p_T < 30$ GeV/c.
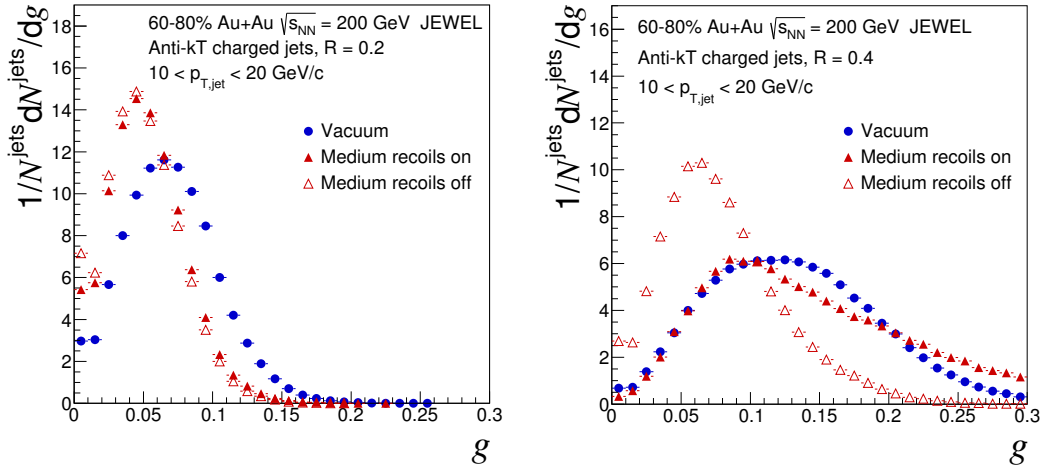

Figure 6.3: Angularity for peripheral Au+Au collisions at $\sqrt{s_{\mathrm{NN}}} = 200$ GeV. $R = 0.2$ (left) and $R = 0.4$ (right) in $10 < p_T < 20$ GeV/c.
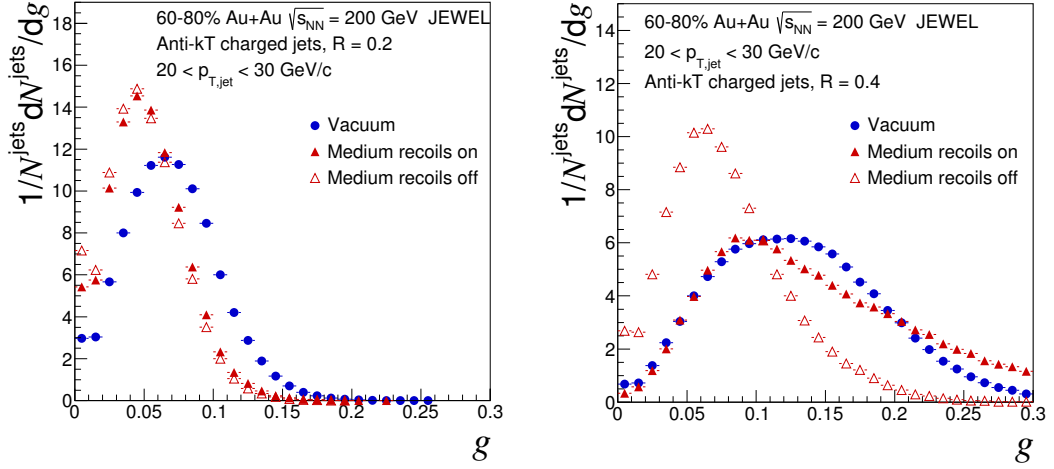
Figure 6.4: Angularity for peripheral Au+Au collisions at $\sqrt{s_{NN}} = 200$ GeV. $R = 0.2$ (left) and $R = 0.4$ (right) in $20 < p_T < 30$ GeV/c.
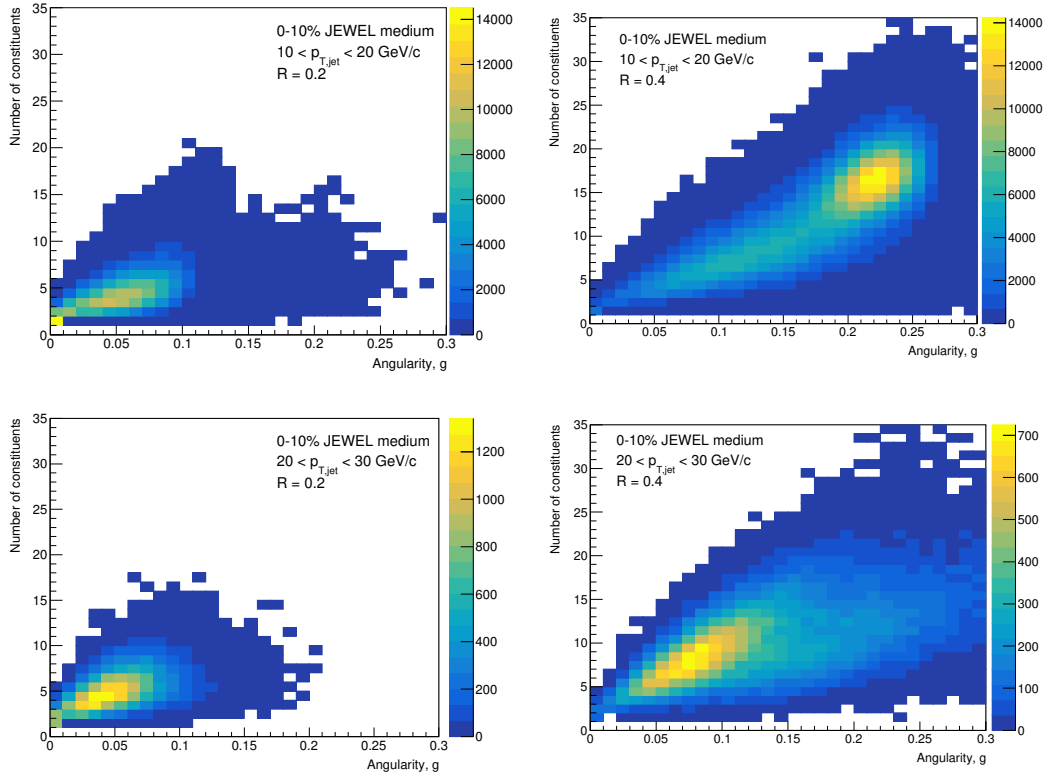

Figure 6.5: 2D statistics for central "recoils on" Au+Au collisions at $\sqrt{s_{NN}} = 200$ GeV with $R = 0.2$ (left) and $R = 0.4$ (right) in $10 < p_T < 20$ GeV/c and $20 < p_T < 30$ GeV/c simulated with medium model.
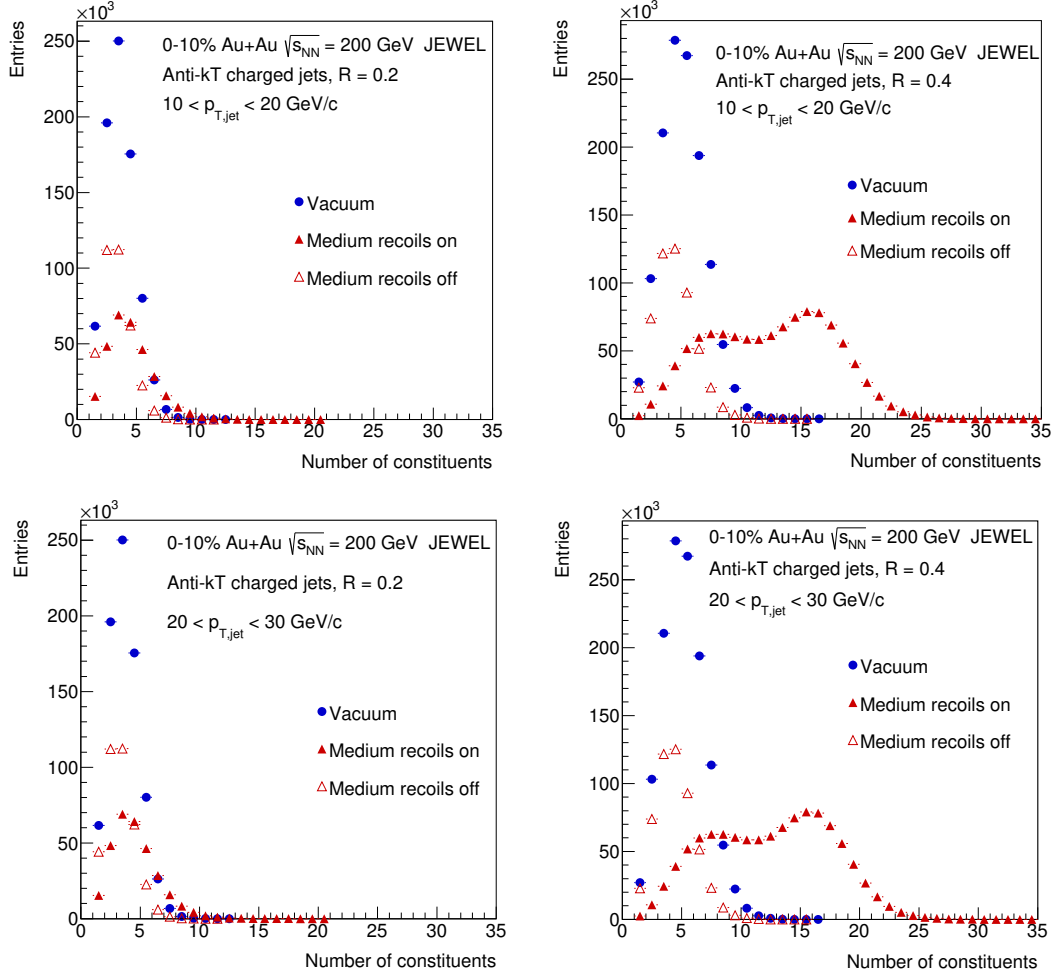
Figure 6.6: Statistics for central Au+Au collisions at $\sqrt{s_{\mathrm{NN}}} = 200$ GeV with $R = 0.2$ (left) and $R = 0.4$ (right) in $10 < p_T < 20$ GeV/c (upper row) and $20 < p_T < 30$ GeV/c (lower row).

6.2 Momentum dispersion

The momentum dispersion was calculated using the Equation (2.3). A comparison of the $p_T D$ for central and peripheral "recoils on/off" Au+Au collisions in simulation with vacuum and medium model can be examined. It can be seen that all the results have similar behavior as the results from the ALICE experiment (Figure (2.7)). However, in contradiction to the ALICE results, the obtained distributions start form $p_T D = 0$ (for $R = 0.4$ in central and peripheral collisions) and $p_T D = 0.1$ (for $R = 0.2$ in central collisions) instead of $p_T D = 0.3$. That can be a consequence of the use of different centrality ranges. Also a shift of the distribution to lower values for the central medium "recoils on" setting for $R = 0.4$ and $10 < p_T < 20$ GeV/c can be observed.
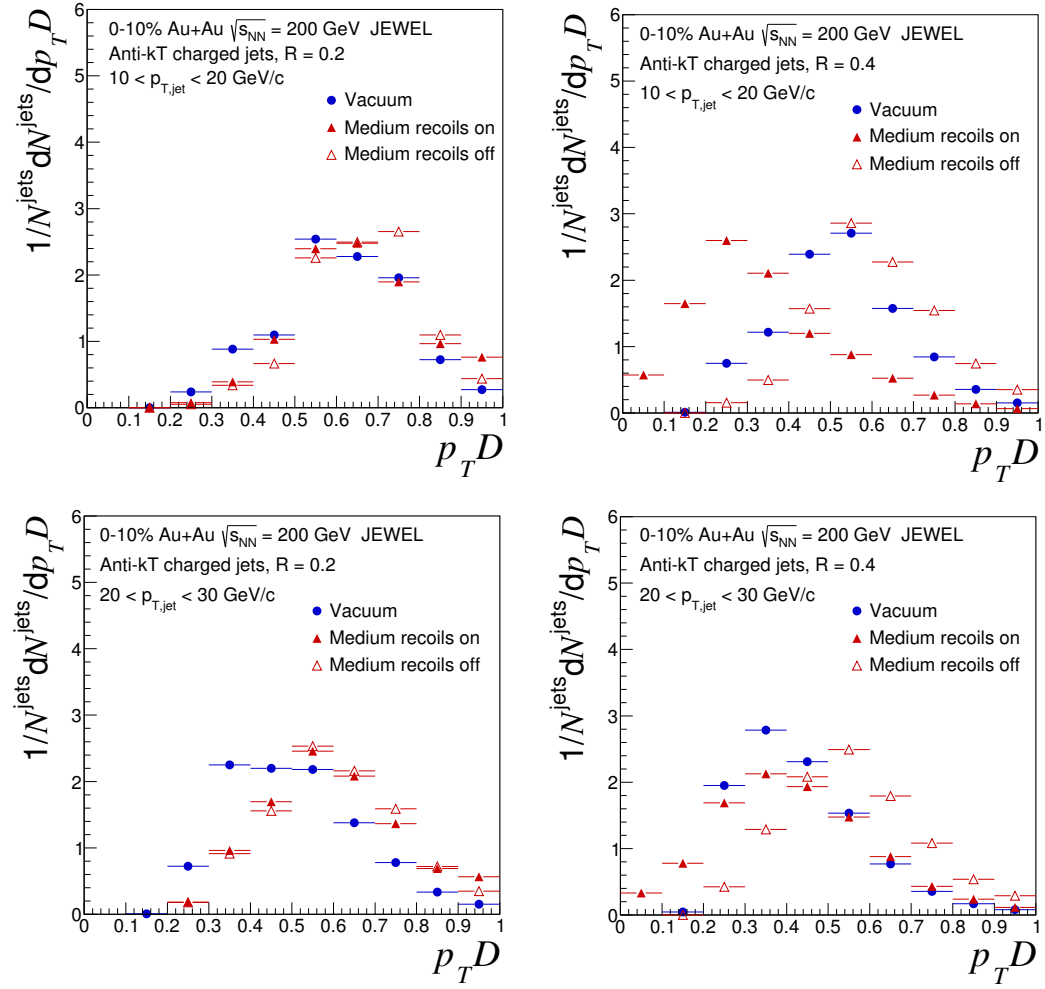
42

Figure 6.7: Momentum dispersion for central Au+Au collisions at $\sqrt{s_{NN}} = 200$ GeV with $R = 0.2$ (left) and $R = 0.4$ (right) in $10 < p_T < 20$ GeV/c and $20 < p_T < 30$ GeV/c .
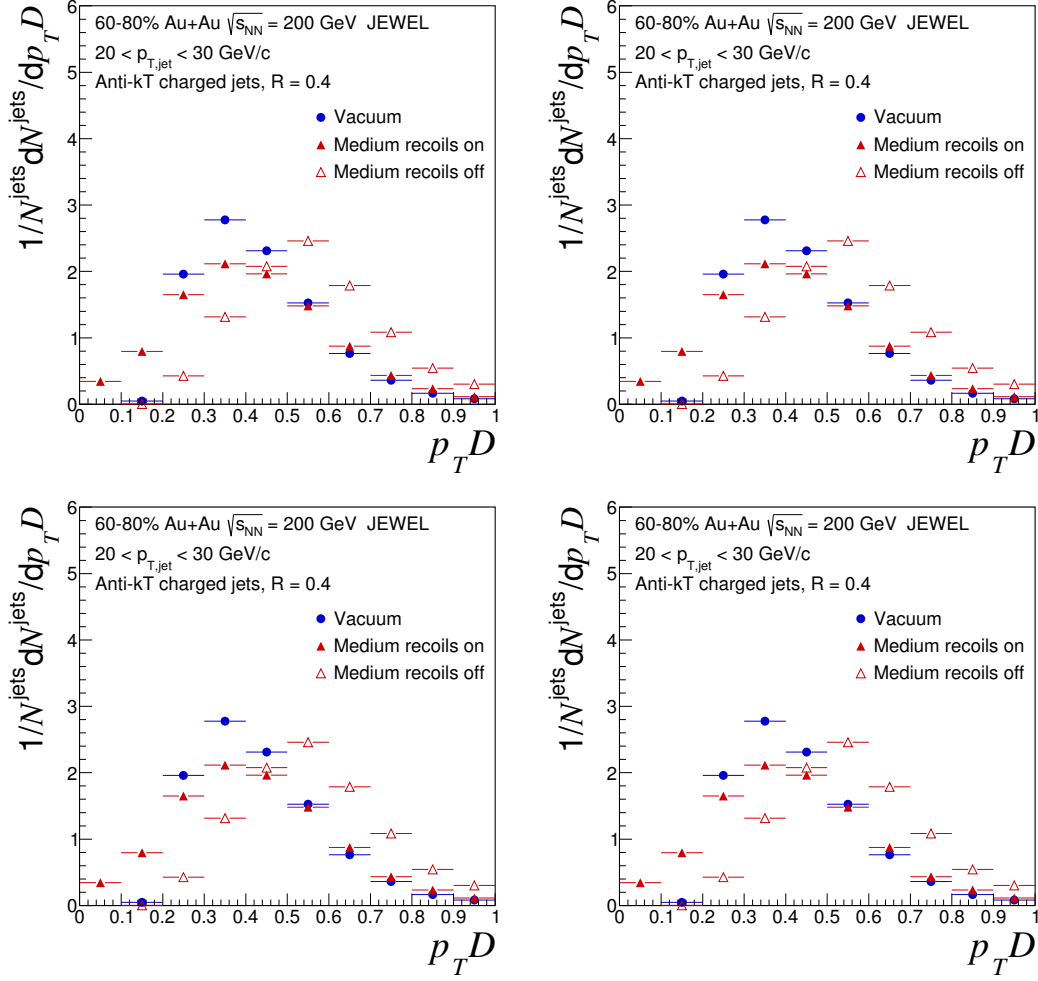
Figure 6.8: Momentum dispersion for Au+Au collisions at $\sqrt{s_{NN}} = 200$ GeV collisions with $R = 0.2$ (left) and $R = 0.4$ (right) in $10 < p_T < 20$ GeV/c and $20 < p_T < 30$ GeV/c .

6.3 LeSub

The *LeSub* was calculated as a difference between the leading and sub-leading p_T tracks (Equation (2.4)). Figure (6.9) performs the *LeSub* distributions for central "recoils on/off" Au+Au collisions for medium and vacuum models. The obtained results have the analogous behaviour to the results from the ALICE experiment (Figure (2.7)).One of the goals of future work is to perform the background subtraction similarly to the ALICE experiment. It is expected that after the background subtraction the points for medium "recoils on/off" and vacuum models will be closer to each other. A similar behavior can be seen in Figure (6.10) for peripheral "recoils on/off" Au+Au collisions for medium and vacuum models.
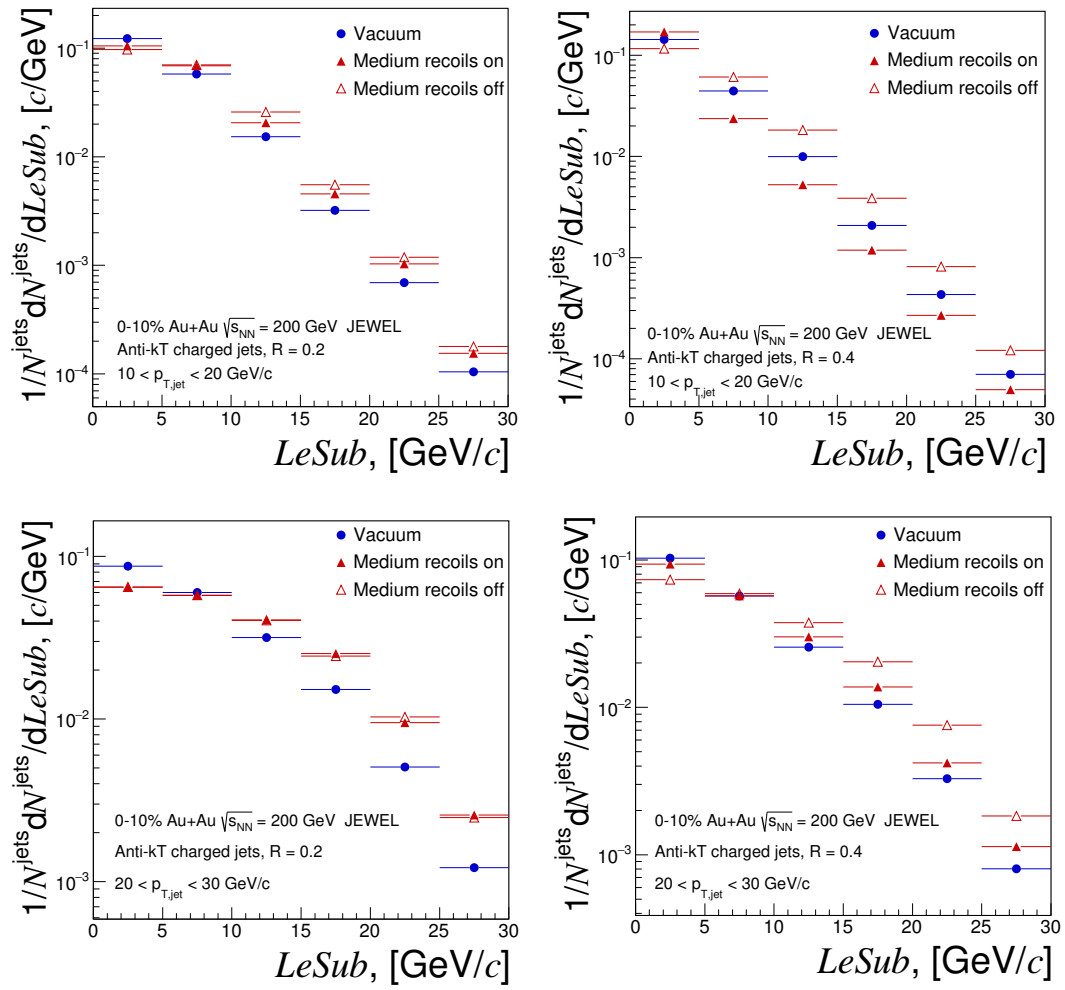
Figure 6.9: *LeSub* for central Au+Au collisions at $\sqrt{s_{\mathrm{NN}}} = 200$ GeV with $R = 0.2$ (left) and $R = 0.4$ (right) in $10 < p_T < 20$ GeV/c and $20 < p_T < 30$ GeV/c .
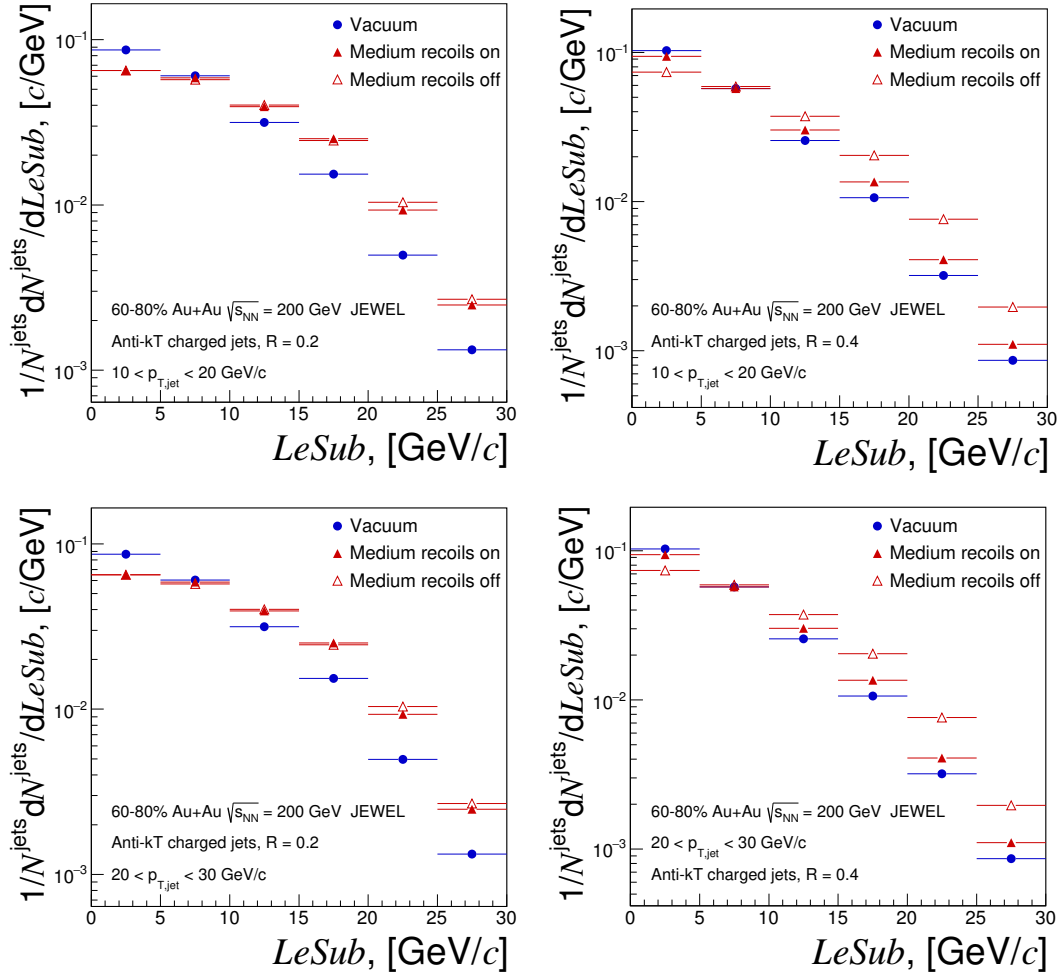
Figure 6.10: *LeSub* for Au+Au collisions at $\sqrt{s_{\mathrm{NN}}} = 200$ GeV collisions with $R = 0.2$ (left) and $R = 0.4$ (right) in $10 < p_T < 20$ GeV/c and $20 < p_T < 30$ GeV/c .

Summary

The nuclear-nuclear collisions at energies attainable at the high energy colliders RHIC at BNL or the LHC at CERN are an ideal environment to study quark-gluon plasma, the hot and dense nuclear matter consisting of free partons. One of the most important probes of this nuclear matter is study of the jet production. This research thesis is focused on the QGP that is produced in the initial stages of heavy-ion collisions at RHIC, mainly at the STAR experiment.

The first chapter of the thesis is an introduction to physics of nucleus-nucleus collisions, where a phase diagram of nuclear matter was described. The chapter also describes the space time evolution of the nucleus-nucleus collisions and the collision centrality. The second chapter gives a brief overview of recent measurements of jets at the LHC. In the chapter the jet shapes used in the following simulation analysis are also described. The third chapter of the thesis is dedicated to the STAR experiment at RHIC. The chapter contains the description of the whole detector system at STAR with a special focus on detectors relevant for jet studies: the Time Projection Chamber, the Time Of Flight system, the Barrel-Electromagnetic Calorimeter and the Heavy Flavor Tracker. The chapter four is mainly devoted to the anti-kT algorithm description needed for the jet analysis. The chapter also contains a brief information about the kT algorithm needed for the future background subtraction and the FastJet software package including these algorithms. The next chapter of the thesis is dedicated to the JEWEL Monte Carlo generator used in the analysis. The simulation parameters used for central and peripheral collisions in vacuum model and for central and peripheral "recoils on/off" collisions in medium model can be also found in the fifth chapter.

The practical part of the work was focused on application of anti-kT algorithm implemented in the FastJet package to the data simulated by JEWEL Monte Carlo generator. The jets were studied using three jet shape observables: angularity, momentum dispersion and *LeSub*. The obtained results are summarized in the sixth chapter and the Appendix C of the thesis. All the results have the same behaviour as the results form ALICE collaboration. It was also shown that the spike in angularity results for $g = 0.01$ in $10 < p_T$ 20 GeV/c for both values of resolution parameters is due to the presence of jets with only one constituent.

This jet shape analysis is the first to be accomplished at STAR. The goals for the future work are to perform the background subtraction similarly to the ALICE experiment (see Subsection 2.3), to apply methods on experimental data and to compare the obtained results with the simulation made in JEWEL and the results from the LHC collaborations.

Appendix A

Basic kinematic observables

In order to describe the properties of particles created in nuclear-nuclear collisions, it is good to define some variables accounting for relativistic effects.

A.1 Transverse momentum

The importance of the transverse momentum arises because momentum along the beamline may just be left over from the beam particles, while the transverse momentum is always associated with whatever physics happened at the collision vertex.

The *transverse momentum p_T* is defined as

$$p_{\mathrm{T}} = \sqrt{p_x^2 + p_y^2}, \tag{A.1}$$

where the p_x and p_y are the components of the three-momentum $\overrightarrow{p} = (p_x, p_y, p_z)$, the last component, p_z, is the component of the momentum along the beam axis (longitudinal momentum p_L).

A.2 Rapidity and pseudorapidity

The *rapidity*, y, is a measure of velocity. It is defined is

$$y = \frac{1}{2} \ln \left(\frac{E + p_L}{E - p_L} \right), \tag{A.2}$$

where p_L is the longitudinal momentum and E is the energy of the particle. The rapidity is related to the angle between the XY plane and the direction of emission of a product of the collision. That means, the the rapidity is zero when a particle is close to transverse to the beam axis, but tends to $\pm\infty$ when a particle is moving close to the beam axis in either direction.

As the rapidity can be hard to measure for highly relativistic particles, the *pseudorapidity*, η, is usually used in experimental particle physics instead of rapidity y. The pseudorapidity is determined by the following equation:

$$\eta = -\ln \left(\tan \frac{\theta}{2} \right), \tag{A.3}$$

where θ is the angle between the particle three-momentum $\vec{p}$ and the positive direction of the beam axis. In comparison to rapidity, pseudorapidity depends only on the polar angle of the particle's trajectory, and not on the energy of the particle. The dependence of the pseudorapidity on the polar angle is shown in the Figure A.1.
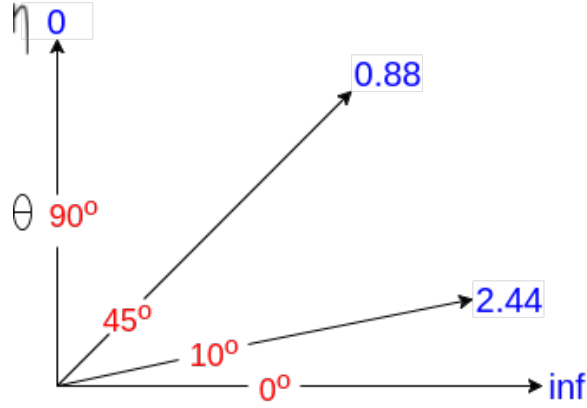

Figure A.1: The dependence of the pseudorapidity η (blue) on the polar angle θ (red). As polar angle approaches zero, pseudorapidity becomes infinite.

A.3 Center-of-mass energy

The *center-of-mass energy*, CMS energy, which is defined as

$$\sqrt{s} = \sqrt{(E_1 + E_2)^2 - (p_1 + p_2)^2}, \tag{A.4}$$

is an energy of the two colliding nucleons with momenta p_1, p_2 and energies E_1, E_2.

$\sqrt{s_{\mathrm{NN}}}$ is the CMS energy per nucleon. In case of a symmetric collision, the relation between previously defined CMS energies is $\sqrt{s_{\mathrm{NN}}} = \sqrt{s}/A$, where A is a nucleon number.

Appendix B

Glossary

- **The Underlying Event (UE)** corresponds to all particles in an event that are not produced directly by the hard scattering of partons. There is a contribution of UE particles emitted in the jet cone to the reconstructed jet p_T [].

- **Infrared and Collinear safe algorithm** - the algorithm's property that if one modifies an event by a collinear splitting or the addition of a soft emission, the set of hard jets that are found in the event should remain unchanged [40].

- **The Parton Distribution Function** is the distribution function is defined as the probability density for finding a particle with a certain longitudinal momentum fraction x at resolution scale $Q2$, where $Q2$ is the energy scale of the hard interaction. The precise knowledge of proton PDF is essential for making predictions for the Standard Model and beyond the Standard Model processes at hadron colliders [41].

- **Landau-Pomeranchuk-Migdal effect**, or simply LPM effect, is a reduction of the bremsstrahlung and pair production cross sections at high energies or high matter densities.

Appendix C

Statistic results

In the appendix the results of statistics for vacuum simulation and for central recoils off and peripheral recoils on/off collisions with medium are presented.
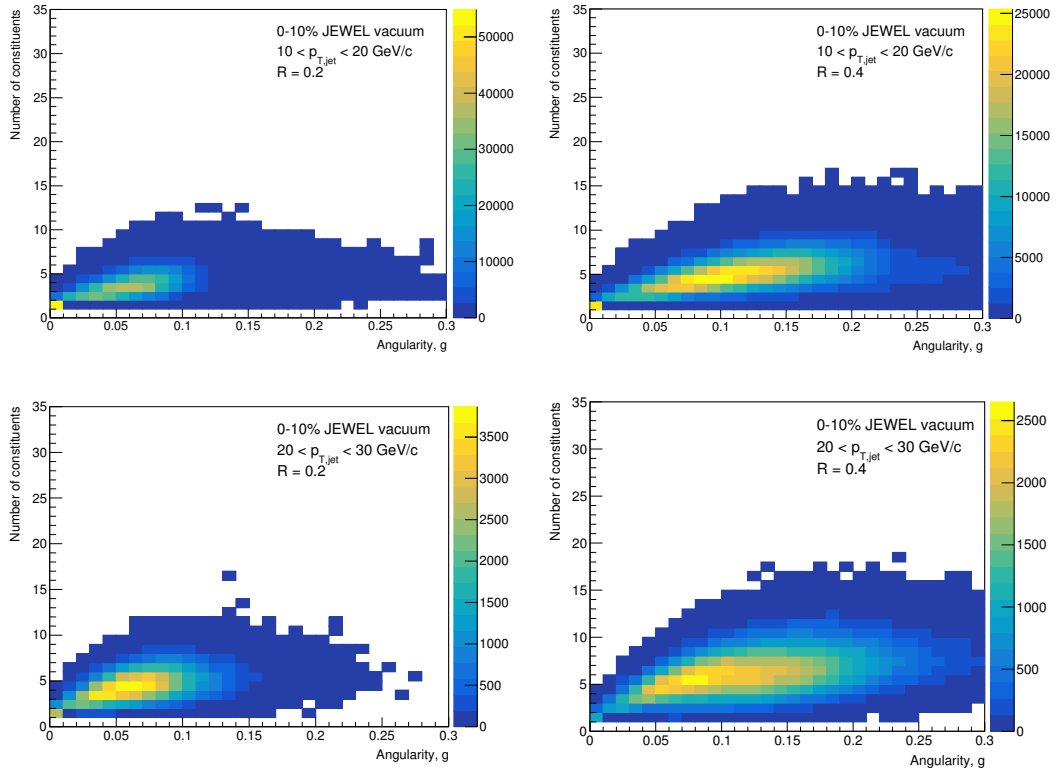

Figure C.1: Statistics for central collisions with $R = 0.2$ (left column) and $R = 0.4$ (right column) in $10 < p_T < 20$ GeV/c (upper row) and $20 < p_T < 30$ GeV/c (lower row) in vacuum model.

Figure C.2: Statistics for peripheral collisions with $R = 0.2$ (left column) and $R = 0.4$ (right column) in $10 < p_T < 20$ GeV/c (upper row) and $20 < p_T < 30$ GeV/c (lower row) in vacuum model.
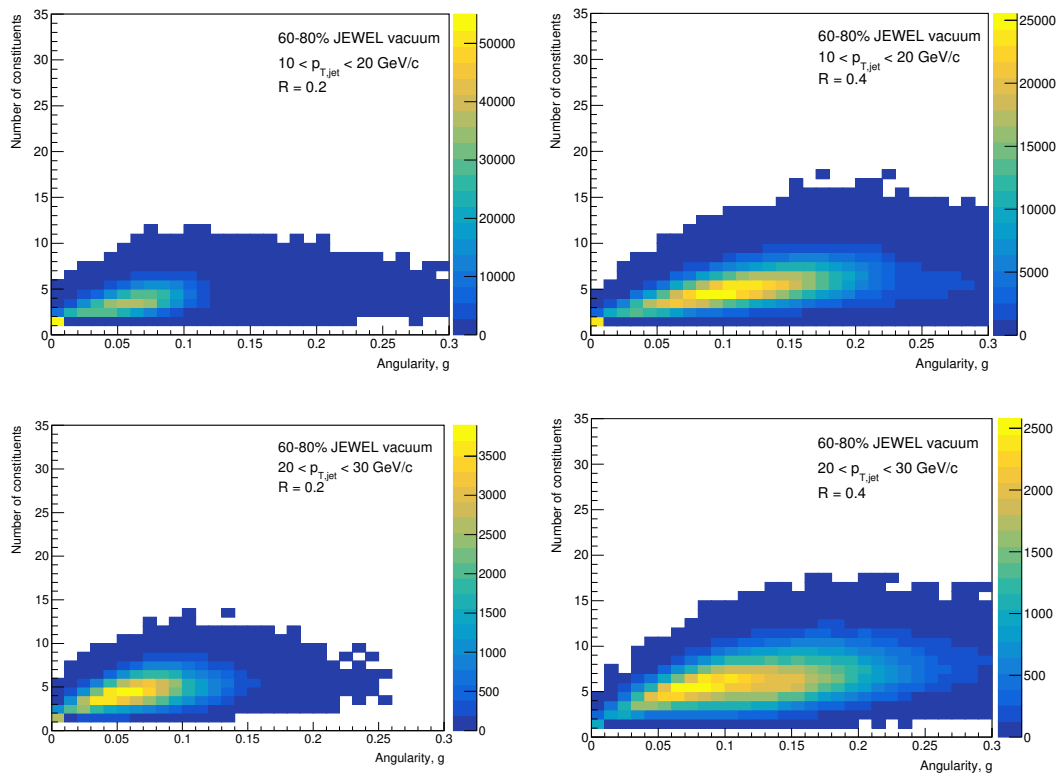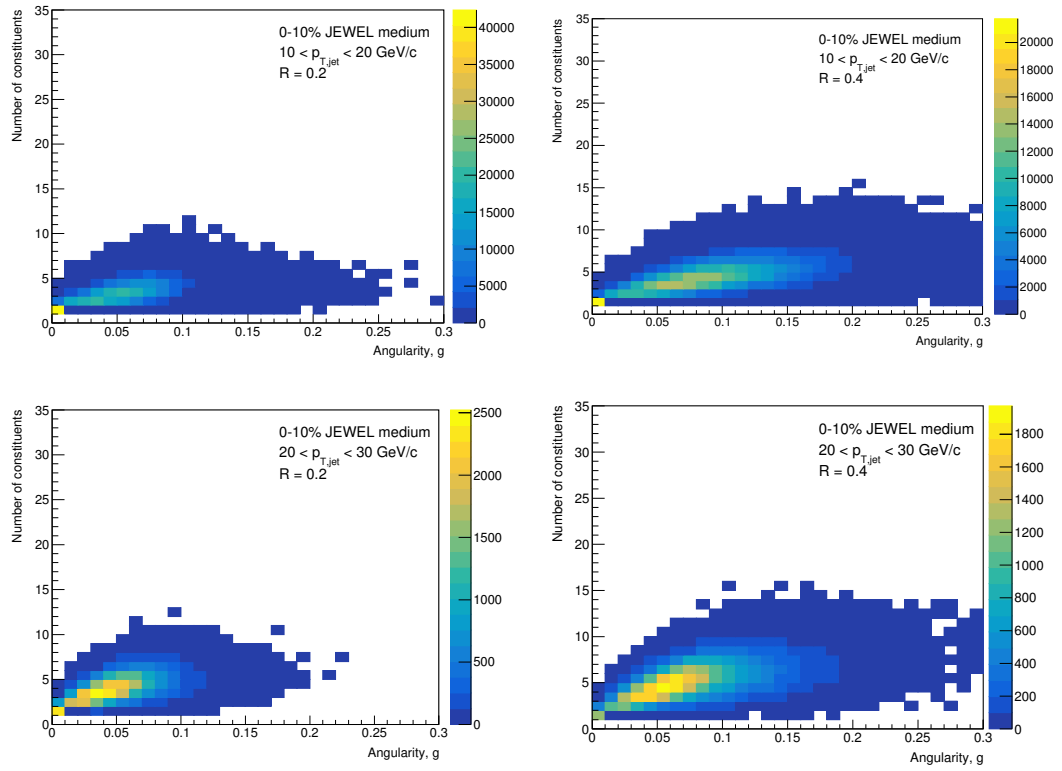
Figure C.3: Statistics for central "recoils off" collisions with $R = 0.2$ (left column) and $R = 0.4$ (right column) in $10 < p_T < 20$ GeV/c (upper row) and $20 < p_T < 30$ GeV/c (lower row) in medium model.

Figure C.4: 2D statistics for peripheral "recoils on" Au+Au collisions at $\sqrt{s_{\mathrm{NN}}} = 200$ GeV collisions with $R = 0.2$ (left column) and $R = 0.4$ (right column) in $10 < p_T < 20$ GeV/c (upper row) and $20 < p_T < 30$ GeV/c (lower row) in medium model.

Figure C.5: 2D statistics for peripheral "recoils off" Au+Au collisions at $\sqrt{s_{\mathrm{NN}}} = 200$ GeV collisions with $R = 0.2$ (left column) and $R = 0.4$ (right column) in $10 < p_T < 20$ GeV/c (upper row) and $20 < p_T < 30$ GeV/c (lower row) in medium model.
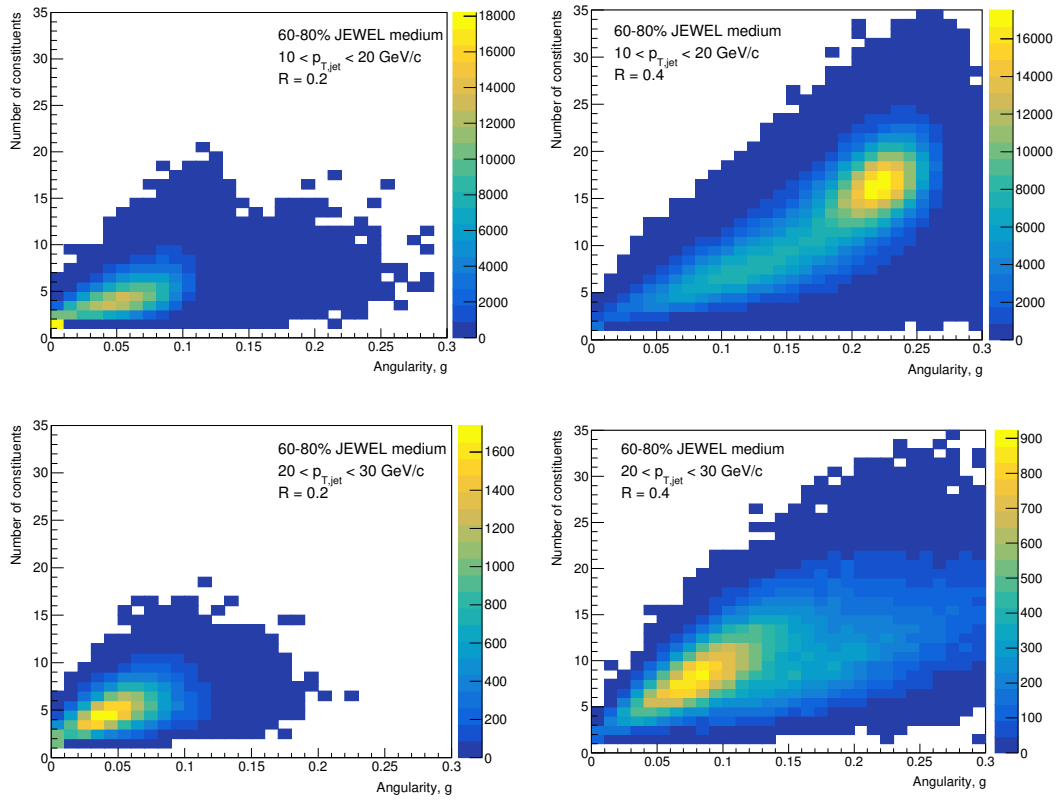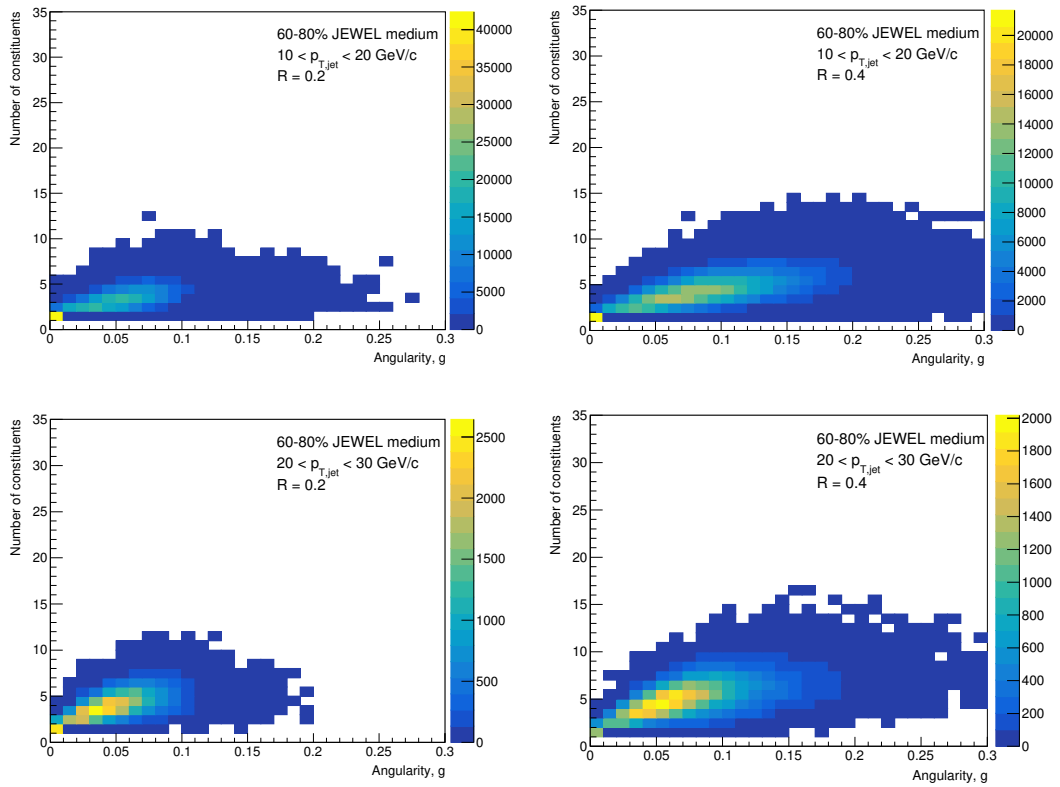
Bibliography

[1] S. Bushwick. How Low Can RHIC Go? `https://www.bnl.gov/today/body_pics/2010/07/phases-of-QCD-350px.jpg`. [online 15.4.2017].

[2] J.D. Bjorken. In *Current Induced Reactions*, Lecture Notes in Physics vol.56. New York: Springer, p.93, 1976.

[3] L.D Landau. Izv. Akad. Nauk SSSR 17, 51; reprinted (1965) in *Collective Papers of L. D. Landau"*, ed. D. T. ter Haar New York: Gordon & Breach, p. 596, 1953.

[4] R. Stock. Relativistic Nucleus-Nucleus Collisions and the QCD Matter Phase Diagram. [arXiv 0807.1610]. 2008.

[5] K. Yagi, T. Hatsuda, Y. Miake. Quark-Gluon Plasma. Cambridge University Press, 2005.

[6] J. Jalilian-Marian R. Venugopalan F. Gelis, E. Iancu. The Color Glass Condensate, *Ann. Rev. Nucl. Part. Sci.* 60, 463-489, 2010.

[7] T. Schuster M. Kliemant, R. Sahoo and R. Stock. Global properties of nucleus–nucleus collisions. In The Physics of the Quark-Gluon Plasma. `http://www.beck-shop.de/fachbuch/leseprobe/9783642022852_Excerpt_001.pdf`.

[8] R. J. Glauber. *Lectures on Theoretical physics"*, vol. 1. New York: Interscience, p. 315, 1959.

[9] S. J. Sanders P. Steinberg M. L. Miller, K. Reygers. Glauber modeling in high energy nuclear collisions, *Ann. Rev. Nucl. Part. Sci.,* 57:205-243, 2007.

[10] F. Tanedo. The picture is taken from:. `http://www.quantumdiaries.org/wp-content/uploads/2011/04/clustering.png`. [online 1.12.2017].

[11] G. Bencedi. Nuclear modification factor of charged particles and light-flavour hadrons in p-Pb collisions measured by ALICE, [arXiv:1609.05665]. pages 285–288, 2016.

[12] G. Aad et al. Measurements of the Nuclear Modification Factor for Jets in Pb+Pb Collisions at $\sqrt{s_{\mathrm{NN}}} = 2.76$ TeV with the ATLAS Detector, *Phys. Rev. Lett.,* 114, 072302, 2015.

[13] S. Salur. A Brief Review of CMS Jet Measurements, *J. Phys. Conf. Ser.* 589(1):012017, 2015.

[14] G. Aad et al. Observation of a Centrality-Dependent Dijet Asymmetry in Lead-Lead Collisions at $\sqrt{s_{NN}} = 2.77$ TeV with the ATLAS Detector at the LHC, *Phys. Rev. Lett.* 105, 252303, 2010.

[15] S. Chatrchyan et al. Observation and studies of jet quenching in PbPb collisions at nucleon-nucleon center-of-mass energy = 2.76 TeV, *Phys. Rev.* C84:024906, 2011.

[16] L. Cunqueiro. Jet shapes in pp and Pb–Pb collisions at ALICE. *Nucl. Phys.*, A956:593–596, 2016.

[17] W. J. Waalewijn A. J. Larkoski, J. Thaler. Gaining (Mutual) Information about Quark/Gluon Discrimination, *JHEP* 11:129, 2014.

[18] S. Acharya et al. Medium modification of the shape of small-radius jets in central Pb-Pb collisions at $\sqrt{s_{\mathrm{NN}}} = 2.76\,\mathrm{TeV}$, *JHEP* 10:139, 2018.

[19] Brookhaven National Laboratory. RHIC. `https://www.bnl.gov/rhic/`. [online 5.5.2018].

[20] Brookhaven National Laboratory. The STAR experiment. `https://www.star.bnl.gov/`. [online 5.5.2018].

[21] B. A. Schwartz C. Grupen. Particle Detectors.

[22] M. Anderson, J. Berkovitz, W. Betts et.al. The STAR Time Projection Chamber: A Unique Tool for Studying High Multiplicity Events at RHIC, [arXiv:nucl-ex/0301015v1], 2003.

[23] M. R. Lomnitz. Ph.D. thesis. Measurement of charmed meson azimuthal anizotropy in Au+Au collisions at $\sqrt{s_{NN}} = 200$ GeV at RHIC (189 pp.). `https://drupal.star.bnl.gov/STAR/files/Dissertation_submit.pdf`.

[24] M. Beddo, E. Bielick, T. Fornek et.al. The STAR Barrel Electromagnetic Calorimeter. `https://www.star.bnl.gov/public/tpc/NimPapers/emc/emc_nim.pdf`, 2002.

[25] Nuclear Science and Technology. `https://nsww.org/projects/bnl/star/trigger-system.php`. [online 13.8.2018].

[26] The Beam-Beam Counter: A Local Polarimeter at STAR. `http://www.star.bnl.gov/~eca/LocalPol/BBCproceeding-Chuck.pdf`. [online 13.8.2018].

[27] W. J. Llope et al. The STAR Vertex Position Detector, *Nucl. Instrum. Meth.*, A759(2014)23-28 .

[28] The RHIC Zero Degree Calorimeters. `https://www.phenix.bnl.gov/~swhite/zcal/index.html`. [online 13.8.2018].

[29] The STAR TOF collaboration. Proposal for a large area Time Of Flight system for STAR. `https://www.star.bnl.gov/public/tof/publications/TOF_20040524.pdf`, 2004.

[30] C. Chasman, D. Beavis, R. Debbe et.al. A Heavy Flavor Tracker for STAR. `http://rnc.lbl.gov/~wieman/hft_final_submission_version.pdf`. [online 6.5.2018].

[31] G. C. Blazey et. al. Run II jet physics, [hep-ex/0005012]. pages 47–77, 2000.

[32] G. Soyez M. Cacciari, G. P. Salam. The Anti-k(t) jet clustering algorithm. *JHEP*, 04:063, 2008.

[33] G. Soyez M. Cacciari, G. P. Salam. The Catchment Area of Jets, *JHEP* 04:005, 2008.

[34] G. Soyez G. Salam. The SISCone Jet Algorithm. `https://siscone.hepforge.org/`.

[35] M. Cacciari, G. P. Salam, G. Soyez. FastJet user manual. [arXiv: 1111.6097]. 2012.

[36] M. Cacciari, G. P. Salam. Dispelling the N^3 myth for the k_t jet-finder. *Phys. Lett.*, B641:57-61, 2006.

[37] K. C. Zapp. JEWEL 2.0.0: Directions for use. *Eur. Phys. J.*, C74(2):2762, 2014.

[38] K. C. Zapp. Geometrical aspects of jet quenching in JEWEL, *Phys. Lett.*, B735:157–163, 2014.

[39] J. Rathsman J. Stachel U.A. Wiedemann K. Zapp, G. Ingelman. A Monte Carlo Model for 'Jet Quenching', *Eur. Phys. J.* C60:617-632, 2009.

[40] G. P. Salam. Towards Jetography, [arXiv: 0906.1140], *Eur. Phys. J.* C67:637–686, 2010.

[41] R. Placakyte. Parton Distribution Functions. [arXiv: 1111.5452], 2011.